Title
Biosphere feedback on regional climate in tropical north Africa

Journal
Quarterly Journal of the Royal Meteorological Society, 123(542)

ISSN
0035-9009

Author
Xue, Y

Publication Date
1997

DOI
10.1256/smsqj.54202

Peer reviewed

Q. J. R. Meteorol. Soc. (1997), **123**, pp. 1483–1515

Biosphere feedback on regional climate in tropical north Africa

By YONGKANG XUE*

Center for Ocean–Land–Atmosphere Studies, Maryland, USA

(Received 8 May 1996; revised 30 September 1996)

SUMMARY

The impact of land-surface degradation over the Sahel area on seasonal variations of atmospheric and hydrological components over tropical north Africa are investigated in a general-circulation model numerical experiment, together with the mechanisms involved. The model was integrated for four years with and without vegetation change over the Sahel region with different initial atmospheric conditions. The results demonstrate that the degradation of the land surface can have a significant impact on the Sahelian regional climate. It increases the surface air temperature and reduces the precipitation, runoff and soil moisture over the Sahel region during the July–August–September (JAS) season. The impact is not only limited to the specified desertification area and the JAS season but is found also to the south of this area and extends into the October–November–December season. The changes in the annual rainfall cycle and the JAS mean surface temperature over the Sahel area are consistent with the observed climate anomalies of the past 40 years. The changes in rainfall to the south of the Sahel including eastern Africa are also in line with the observed anomalies.

The reduction in total diabatic heating rate and relative increase in subsidence motion in the upper troposphere are consistent with the rainfall anomalies. The variations in convective heating rate, which were caused by changes in latent-heat flux from the land surface and moisture flux convergence in the atmosphere, are the dominating factors in this process. The radiative cooling is a secondary effect. The influence of the initial conditions on the simulation of the soil water balance is also analysed.

KEYWORDS: Desertification Land-surface degradation Rainfall Sahel regional climate Soil water balance

1. INTRODUCTION

The African continent has been experiencing land-surface degradation during the past century. Anthropogenic effects, such as over-exploitation of land resources by overgrazing, poor irrigation, and the destruction of woody vegetation, have played an important role in this process. The major desertification processes in northern Africa are manifested in degradation of the vegetation cover and accelerated water and wind erosion (e.g. Gormitz 1985; Dregne and Tucker 1988; Dregne and Chou 1992). According to Dregne and Chou (1992) these processes mainly affect the land uses on rangeland. About 74% of rangeland is desertified, with 71% severely desertified.

A number of studies with different models have been conducted to study the role of biosphere feedback on the Sahel drought of the past 20 years. In the earlier studies, simple surface-layer models were used for sensitivity studies. Only a single land-surface parameter was tested each time. The primary factors of the desertification under investigation were surface albedo, soil moisture, and surface roughness length. These studies revealed that higher surface albedo, less soil moisture, and lower surface roughness length would lead to lower precipitation in Africa (e.g. Charney *et al.* 1977; Walker and Rowntree 1977; Sud and Fennessy 1982; Cunnington and Rowntree 1986; Laval and Picon 1986; Kitoh *et al.* 1988; Sud *et al.* 1988).

Real atmosphere–biosphere interaction processes are, however, much more complex and involve many parameters. Therefore, sophisticated land-surface models are needed to assess realistically the impact of desertification on the Sahel drought. A proper evaluation

* Corresponding address: Department of Geography, University of Maryland, College Park, MD 20742, USA.

of the surface feedback to climate can be obtained only when all comparable components of the energy and water balances are considered. Models such as the Biosphere–Atmosphere Transfer Scheme (Dickinson *et al.* 1986) and the Simple Biosphere model (SiB, Sellers *et al.* 1986), each of which has an elaborate and biologically realistic representation of land-surface processes, have been developed with the help of the further understanding of surface micrometeorology in the presence of vegetation. Satellite observations have also provided much of the land-surface information required by these biosphere models. A number of Sahel drought studies have been conducted using coupled biosphere–atmosphere models (Xue *et al.* 1990; Xue 1991; Xue and Shukla 1993; Diedhiou and Mahfouf 1995; Xue and Shukla 1996). Unlike previous studies, these coupled models are able to simulate observed decadal rainfall anomalies over the desertified Sahel region. These studies show the following causes of the reduction of simulated Sahelian summer rainfall in the desertification experiments: the reductions in evapotranspiration and moisture flux convergence, the shifting of the summer monsoon rain belt to the south, the suppression of easterly wave disturbances, and the changes in other atmospheric components. The coupled model provided further insight into biosphere–atmosphere interaction mechanisms.

In addition to the land-surface effects, observational and model studies have revealed that sea surface temperature (SST) anomalies are highly relevant to the seasonal to interannual rainfall variability in northern Africa (Lamb 1978; Palmer 1986; Nicholson and Entekhabi 1986; Semazzi *et al.* 1988; Folland *et al.* 1991; Lamb and Peppler 1991; Xue and Shukla 1993; Shinoda and Kawamura 1994; Rowell *et al.* 1995). In Rowell *et al.* (1995) a set of general-circulation model (GCM) simulations were performed aimed at simulating July–August–September (JAS) rainfall anomalies for ten selected years between 1949 and 1990. In each experiment the GCM was forced by the observed SST pattern for the appropriate year. The model simulates the magnitude and patterns of JAS rainfall anomalies across tropical north Africa very well. However, these results were not confirmed by their integrations with a later version of the model or by other GCM groups (Sud and Lau 1996). After improving the model, Rowell (1996) again showed high correlations between the SST and observed rainfall anomalies, but the correlations were not as large as in their earlier work. The land surface-moisture feedback was also investigated in their study using a simple soil-moisture scheme. The impact was limited. To investigate the causes of Sahel drought comprehensively, the effects and mechanisms of SST and land-surface processes need to be further investigated separately and jointly with different models.

To advance our understanding of the impact and mechanisms of land-surface degradation on the climate anomalies over tropical northern Africa gained with a previous study (Xue and Shukla 1993), four-year integrations using the Center for Ocean–Land–Atmosphere Studies (COLA) GCM were conducted. Climatological SST was specified as the lower atmospheric boundary condition over the ocean in this study. No experiment was designed to test the effect of SST anomalies. In Xue and Shukla's (1993) study the integration period was only three months. Although the influence of initial conditions for some variables only lasts a relatively short period of time, the memory for others, such as soil moisture, is much longer. The effects of such memory have been questioned and have yet to be tested (Rowell *et al.* 1995). In addition to the summer rainfall anomalies over the Sahel, the impact of land-surface processes on the annual cycle of other atmospheric and hydrological variables and other parts of the African continent also need to be investigated. Specifically, longer-term integrations and large samples are necessary to establish the statistical significance of the results.

In this paper the model is briefly described in section 2. The experimental design is described in section 3. The simulation results are presented in sections 4, 5, 6 and 7. Section 8 is the discussion and summary.

2. Model description

The COLA GCM is based on a modified version of the National Centers for Environmental Prediction (formerly National Meteorological Center) global spectral model with rhomboidal truncation at zonal wave number 40 (Sela 1980; Kinter *et al.* 1988; Sato *et al.* 1989; Fennessy *et al.* 1994). The prognostic computations are carried out in the spectral domain and the physical processes are computed on a Gaussian grid (with approximately 1.8° latitude by 2.8° longitude resolution). The model is partitioned into 18 vertical layers. A 'mean orography' was computed on the COLA GCM Gaussian grid from the US Navy 1/6° resolution model terrain-height data. The parametrizations of the physical processes include:

(i) An efficient radiation scheme that resolves the diurnal cycle and includes terrestrial radiative heating (Harshvardhan *et al.* 1987) and solar radiative heating (Lacis and Hansen 1974, modified by Davies 1982). An interactive cloud scheme, similar to the one developed by Slingo (1987), was incorporated into the GCM for the radiation calculations (Hou 1990).

(ii) The level 2.0 second-order turbulence closure scheme of Mellor and Yamada (1982) for subgrid-scale exchanges of heat, momentum and moisture.

(iii) A modified Kuo scheme for convection (Kuo 1965), shallow convection (Tiedtke 1984), and large-scale condensation.

(iv) A gravity-wave-drag parametrization which follows that of Alpert *et al.* (1988).

The Simplified SiB (SSiB) model (Xue *et al.* 1991, 1996a, 1996c) is used to model the land surface in the COLA GCM. The SSiB model has three soil layers, one canopy layer, and eight prognostic variables: volumetric soil moisture content (VSMC) in three soil layers; temperature at the canopy, ground surface and deep soil layers; water stored on the canopy; and snow stored on the ground.

In the soil layers water movement is described by a finite-difference approximation to the diffusion equation. The force–restore method is used to predict the time variation of soil temperature. The governing equations for the interception of water stores are based on water-conservation equations.

There are 12 vegetation types in the SSiB, comprising: tall vegetation (tropical rainforest, broadleaf deciduous trees, broadleaf and needle-leaf trees, needle-leaf evergreen trees, needle-leaf deciduous trees, and savannah); short vegetation (grassland, broadleaf shrubs with ground cover, shrubs with bare soil, and dwarf trees with ground cover); arable crops; and bare soil (Dorman and Sellers 1989). A parameter-set was created for each of the 12 SSiB vegetation types based on a variety of sources. Most parameters were derived from the biometric and physiological data for representative species in each biome determined from a wide range of surveys in the ecological and geographical literature (Willmott and Klink 1986; Dorman and Sellers 1989), while others were derived from calibration and validation studies (Sellers *et al.* 1989; Xue *et al.* 1996a, b). Many parameters are invariant with season. Except for crops, seasonally varying monthly values of leaf-area index and green-leaf fraction are prescribed.

The main sources of data for the distribution of the world vegetation types are the physiognomic classification of Kuchler (1983) and the land use database of Matthews (1984, 1985), which have been used to compile a world vegetation map. One vegetation type is specified at each model grid point. The African vegetation map is shown in Fig. 1. In the COLA GCM, SSiB parameters are assigned to each grid square based on the input vegetation-map and month. The surface model provides the GCM with land–atmosphere fluxes of latent heat, sensible heat, momentum, and radiation.

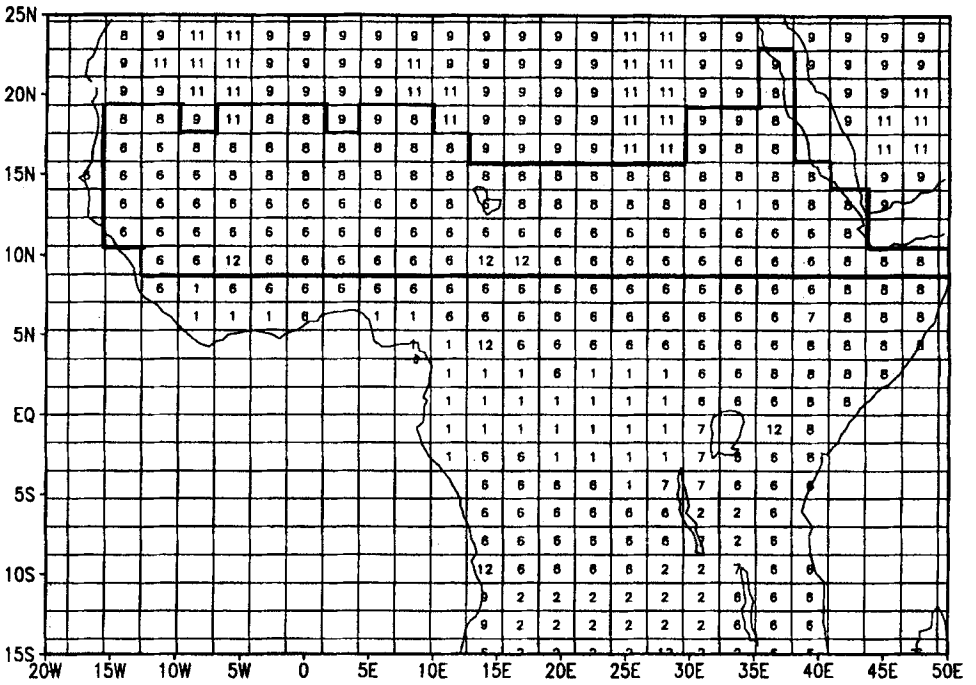

Figure 1. Vegetation-type map for control run. Type 1 is tropical rainforest, 2 is broadleaf deciduous trees, 6 is savannah, 7 is grassland, 8 is broadleaf shrubs with ground cover, 9 is shrubs with bare soil, 11 is bare soil and 12 is crops. In the area enclosed by the dark line the vegetation types are changed to type 9 for the desertification experiment.

The version of the COLA GCM used in this study is an improvement of the one used in Xue and Shukla (1993). The main new features in this version are gravity-wave drag and a mean topography (Fennessy *et al.* 1994).

3. Experimental design for desertification

There are controversies concerning the definition of desertification as well as the scope of the land-surface degradation on the African continent. Based on aerial photographs and satellite observations, it has been argued that the desertification process has been exaggerated or may not even exist in some parts of the African continent (e.g. Hellden 1991). Although it is not the purpose of this paper to resolve this issue, some clarification is necessary.

One phenomenon which must be distinguished from desertification is the vegetation biomass change caused by natural precipitation variations which have a large interannual component. The vegetation biomass is less in dry years compared with that in wet years. But this kind of interannual variation is not the subject of this study.

Desertification in this paper refers to the degradation of land form and the destruction and conversion of vegetation cover and type, which has occurred during the past 40 years mainly because of human activity. This kind of change has been reported in many papers (e.g. Gormitz 1985; Dregne and Tucker 1988; Dregne and Chou 1992). In a recent survey (Akhtar-Schuster 1995) it was found that the vegetation composition and type have been substantially changed in Butana, Sudan, over the past 40 years, coincident with an increase

TABLE 1. VEGETATION PARAMETERS FOR THREE VEGETATION TYPES

	Type 6	Type 8	Type 9
Mean surface albedo	0.20	0.20	0.28
Roughness length* (m)	0.81, 0.75, 0.95, 0.91	0.24, 0.20, 0.25, 0.26	0.06, 0.06, 0.06, 0.06
Leaf-area index*	1.58, 1.27, 4.12, 2.83	0.53, 0.27, 0.86, 0.82	0.94, 0.34, 0.31, 0.71
Greenness*	0.60, 0.68, 0.81, 0.64	0.56, 0.57, 0.70, 0.65	0.60, 0.49, 0.71, 0.89
Minimum stomatal resistance ($s\ m^{-1}$)	282	1041	1041
Vegetation cover	0.3	0.1	0.1
Total depth of three soil layers (m)	3.5	1.5	1.5
Hydraulic conductivity of saturated soil ($m\ s^{-1}$)	0.2E − 4	0.176E − 3	0.176E − 3
Volumetric soil moisture content at the wilting level	0.13	0.05	0.04

Type 6 is savannah.
Type 8 is broadleaf shrubs with ground cover.
Type 9 is shrubs with bare soil.
* The four numbers in each column are the means for January to March, April to June, July to September and October to December, respectively.

in anthropogenic influences. The impact of such decadal changes in vegetation conditions is the subject of this study.

Three control and desertification integrations were conducted. The desertification area in desertification scenarios was the same as in Xue and Shukla (1993), which is close to the severe desertification area in the United Nations Environment Programme's (UNEP) desertification map (UNEP 1992). In the desertification experiment all the vegetation types, except bare soil (type 11), in the specified desertification area were replaced by shrubs with bare soil (type 9) as in Xue and Shukla (1993, see Fig. 1). This more or less reflects the degradation of vegetation and soil and the conversion of vegetation types in this area. The main vegetation types in this region are savannah (type 6) and broadleaf shrubs with ground cover (type 8). At this stage there are still no quantitative data available which can provide land-surface degradation information over the entire Sahel. In this sensitivity study the land-surface degradation was exaggerated to obtain more statistically significant results. Table 1 contains a list of the major surface parameters for types 6, 8 and 9.

The changes in vegetation and soil properties in the desertification experiment took place over the entire year. The prescribed leaf-area index, greenness, and surface roughness length have monthly variations and their seasonal mean values are listed in Table 1. The vegetation parameters for each vegetation type in the model were intended to represent average conditions and, as mentioned above, were based on a variety of sources. Recent observations indicate that there is little vegetation between December and May in some parts of the Sahel (Wallace *et al.* 1992; Goutorbe *et al.* 1994). Thus the changes prescribed for the desertification experiments during this period are probably unrealistic. This causes some problems in the numerical experiments, which will be discussed later. Because the vegetation parameters in the SSiB are prescribed and do not interact with the climate, the impact caused by the feedback processes may be underestimated.

Atmospheric initial conditions on 1 June, 2 June and 3 June 1988 were used for each of the three pairs of ensemble runs as shown in Table 2. The cases with climatological land-surface properties are labelled 'C' and those for desertification runs 'D'. The model was integrated from June 1988 for 43 months in cases C1 and D1, and from June 1988

TABLE 2. GCM EXPERIMENTAL DESIGN

Case	Initial conditions	Months of integration	Land-surface conditions over Sahel
C1	1 June 1988	43	Climatology
D1	1 June 1988	43	Desertification
C2	2 June 1988	31	Climatology
D2	2 June 1988	31	Desertification
C3	3 June 1988	31	Climatology
D3	3 June 1988	31	Desertification

for 31 months in cases C2, D2, C3, and D3; the former period includes four and the latter period three Sahel rainy seasons. Integrations for cases C1 and D1 were extended for one more year to investigate the ground-water balance, and further explanations are in section 6. The ensemble means of C1, C2, and C3, and of D1, D2, and D3 are referred to as ensembles C and D respectively. Results for the last year in C and D were from only one case, C1 and D1 respectively. As mentioned above, the climatological SST was the boundary condition specified in all these integrations.

4. IMPACT ON THE PRECIPITATION

The rainfall deficit has been the most significant climate anomaly in the Sahel area during the past 40 years. The Sahel area has been experiencing drought since the late 1960s after a wetter decade in the 1950s. Temporal and spatial characteristics of the Sahel rainfall variability have been extensively investigated for many years (e.g. Lamb 1978; Nicholson 1981; Folland *et al.* 1991; Lamb and Peppler 1991; Nicholson and Palao 1993; Rowell *et al.* 1995). These studies have shown that low-frequency variations were dominant in the Sahelian rainfall variability. However, rainfall records from 1900 to 1990 revealed that, although there were several dry years before the 1950s, there was no distinct period with longer-term drought resembling the rainfall decline since the 1960s. This study compares rainfall differences between the control and desertification experiments with observed decadal rainfall anomalies over equatorial northern Africa; the major focus is on the Sahel to study the roles of land-surface processes in this drought.

Rainfall data of Nicholson (1993) and Hulme (1992) were compared with the model simulation. Nicholson's station-data were first interpolated to the GCM grid points. The methodology used is an areal weighted averaging technique within the grid box, each grid box being divided into 100 subgrid boxes. The value for each subgrid box was taken from the nearest station within a 2° radius. These values from the 100 subgrid boxes were then averaged to obtain the mean for each grid box. The precipitation maps after gridding were carefully compared with the original station-data and with another precipitation map compiled by Hulme, which was gridded at 2.5° by 3.75° resolution with more sophisticated interpolation. The rainfall map from Nicholson's data and Hulme's map were consistent.

Table 3 lists the observed seasonal rainfall for the region 9°N to 17°N and 15°W to 43°E for January–February–March (JFM), April–May–June (AMJ), July–August–September (JAS), and October–November–December (OND). This area is outlined by bold lines in Fig. 2(b) and will be referred to as the test area. Compared with Fig. 1 it is clear that it covers most of the specified desertification area. The observed precipitation data listed in Table 3 are the climatological data from Nicholson, who averaged all available rainfall data through the 1980s. Some stations had records for over 100 years. The average from 1940 to

TABLE 3. SEASONAL MEAN PRECIPITATION (MM MONTH^{-1}) OVER THE TEST AREA (SEE TEXT)

Season	January to March	April to June	July to September	October to December
Observed climatology	4(3)	47(26)	155(143)	15(11)
Observed difference between 1980s and 1950s	−1(−1)	−7(−5)	−45(−43)	−6(−4)
Simulated precipitation in ensemble C	9	72	130	21
Difference between ensembles D and C	−6	−27	−39	−8

The observational data are from Nicholson (1993) and in parentheses from Hulme (1992).

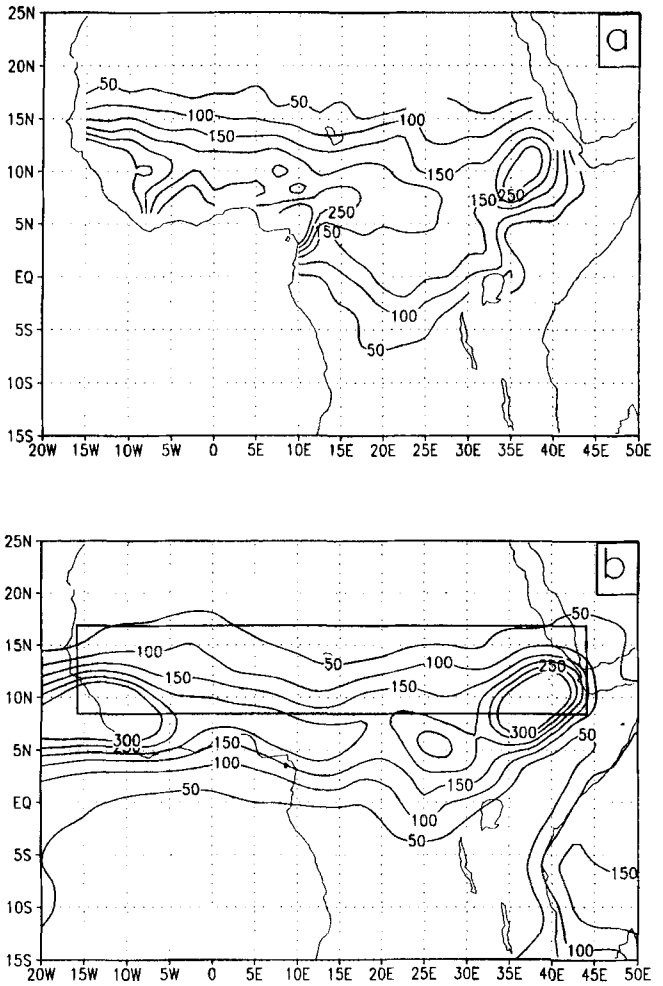

Figure 2. July to September mean precipitation: (a) observed rainfall climatology and (b) ensemble C. Contour interval is 50 mm month^{-1}. The area enclosed by the dark line is referred to as the test area. (See text for further explanation.)

1990 using Hulme's data was also obtained and the results are also shown (in parentheses in the table). Despite different sources and different interpolation schemes, the results from both data sets are reasonably close. The seasonal trend is consistent, although Hulme's climatology data have a slight dry bias. This may be due to the relatively short time-span of his data set, which covered a prolonged dry period. Between these two data sets there is a relatively large difference in the observed AMJ climatology. It is likely that the length of the data set and the number of stations have more impact on this season. This study primarily uses Nicholson's data set since it includes more data over central Africa.

Since climatological SSTs were used as the model boundary condition over ocean, the summer simulations from control integrations were expected to be close to the observed climatology. Figures 2(a) and 2(b) show observed and simulated JAS mean rainfall respectively. The results in Fig. 2(b) are the average of four JAS means in ensemble C. Similar results in this paper show ensemble means.

In a previous study Xue and Shukla (1993) found that the simulated precipitation over the Sahel region was excessive, with the 50 mm month^{-1} isohyet about 2–4° (one or two model grid boxes) north of its observed position. In the new version of the COLA GCM the simulated precipitation over this region is less than that observed during the summer rainy season. The position of the 100 mm month^{-1} isohyet is about 2–4° south compared with its observed climatology. Although the errors in simulating the location of the rainfall belt are very close to the model's horizontal resolution limit, they cause the simulated summer rainfall (in particular in August as will be shown later) to be substantially lower than the observations. This problem illustrates some of the difficulties in modelling the Sahel, where the rainfall is concentrated in a very narrow belt. Overall the JAS rainfall patterns were simulated reasonably well.

After the Sahel rainy season the African Intertropical Convergence Zone (ITCZ) moves to the south. Figures 3(a) and 3(b) show the observed and the control simulated OND rainfall, respectively. The 50, 100, and 150 mm month^{-1} isohyets at the southern boundary of the Sahel region and central Africa are consistent with the observations. The simulated maximum rainfall in central Africa is higher than observations, its extent is much larger, and its location is about 5° east compared with the observations.

Figure 4(a) shows the time series of observed monthly mean rainfall averaged over the test area for the climatology, the means of 1980–89 and 1950–59. For easy comparison with the four-year simulations the observed annual cycle in this figure is repeated four times. The rainy season in the Sahel includes June through September with a peak in August; there is almost no precipitation in the winter. In the 1980s the rainfall deficit mainly occurred during July, August and September.

Simulated monthly mean rainfall over the same area from ensembles C and D is shown in Fig. 4(b). The simulated seasonal mean precipitation is listed in Table 3. Seasonal variations of precipitation over the Sahel area, in both the wet and dry seasons, are well simulated. The simulated JAS rainfall for ensemble C is low, as discussed before, and is close to the observed JAS rainfall in the 1980s, 129 mm month^{-1}. It is clear from Fig. 4(b) that this dry bias is mainly caused by the August rainfall in the control integrations. With the exception of JAS, the model simulates more rainfall than is observed in other seasons, with the AMJ season mean having the largest errors.

The test area was then divided into two sub-regions for further analysis. One sub-region covers the area from 9°N to 13°N and 15°W to 43°E, the other covers the area from 13°N to 17°N and 15°W to 43°E. These will be referred to as area S and area N respectively. Because the rainfall belt did not move northward sufficiently, most of the simulated rainfall deficiency occurred in area S. The observed and simulated JAS rainfall for area S are 207 mm month^{-1} and 193 mm month^{-1} respectively. For area N they are

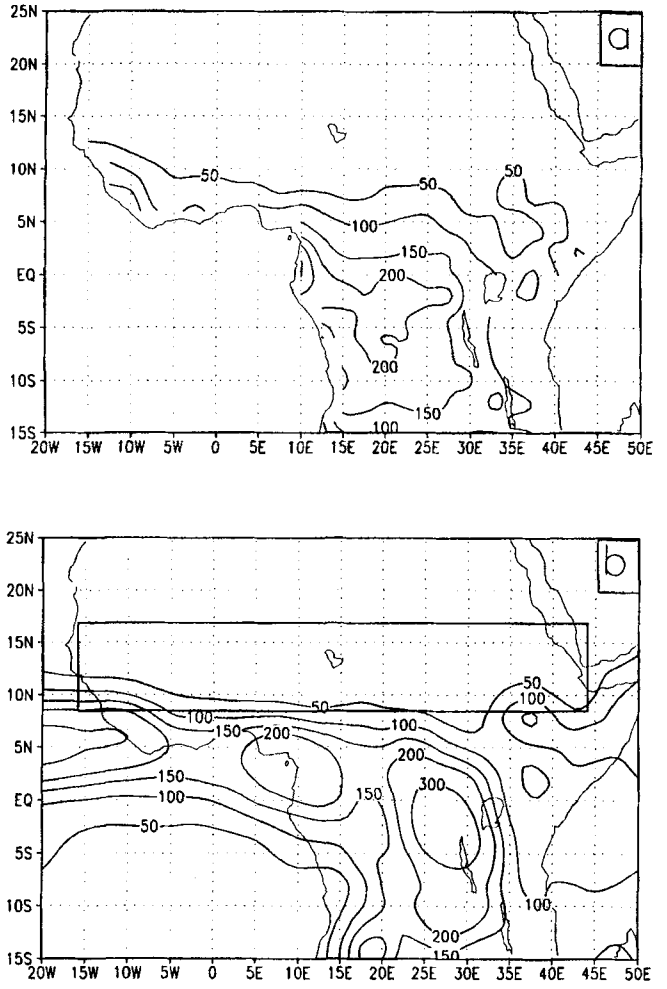

Figure 3. As Fig. 2 but for October to December.

99 mm month^{-1} and 66 mm month^{-1} respectively. The results over areas S and N have many different features which will be discussed.

The results of Xue and Shukla (1993) were from short-term (three months) integrations. The 'memory' of initial atmospheric and soil-moisture conditions affected the results. It was suspected that, after a dry season, the difference in land-surface conditions might have no impact on the atmosphere, because the atmospheric system and soil moisture would start from the same condition (in control and desertification integrations) and the memory of the previous year's rainfall would disappear (Rowell *et al.* 1995). However, the results in Fig. 4(b) demonstrate that, as long as the land-surface degradation exists and the SST conditions remain the same, the simulated summer rainfall anomalies will occur despite the passing of dry seasons.

Observed seasonal mean rainfall differences between the 1980s and 1950s from both the Nicholson (1993) and the Hulme (1992) data sets are listed in Table 3. There appear to be only small differences between these two data sets. In the desertification integrations the model simulates the large rainfall reduction during the JAS rainy season when major

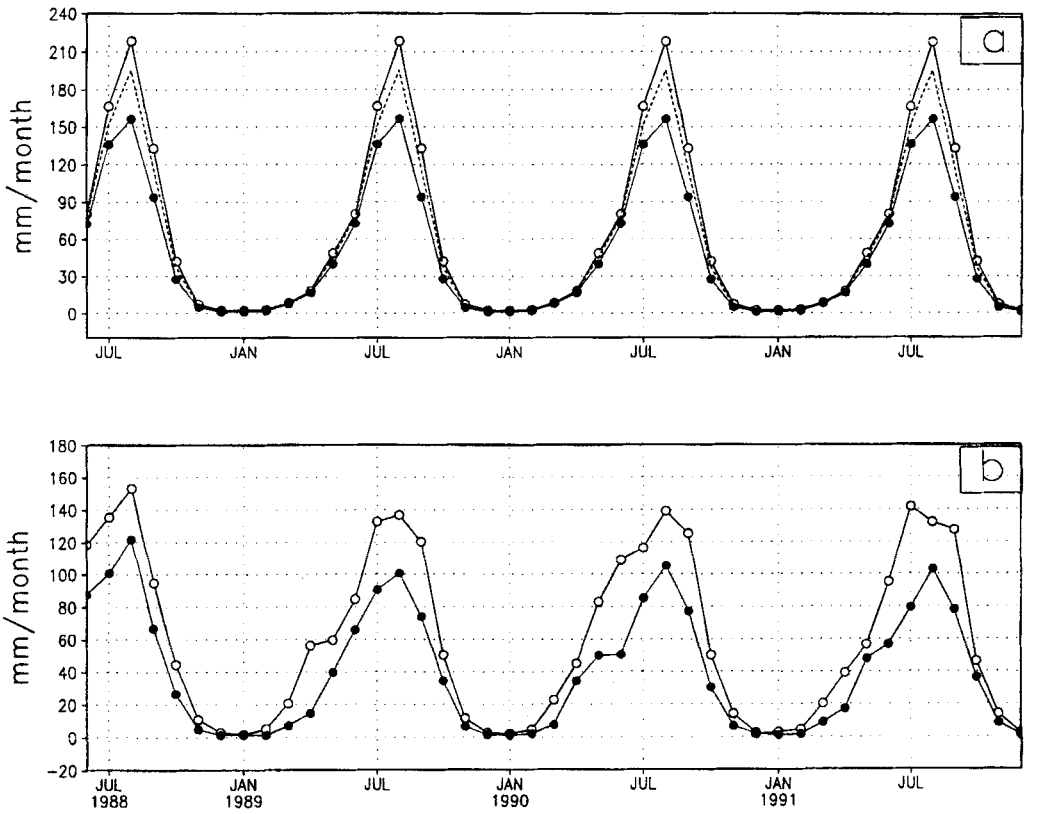

Figure 4. Monthly mean precipitation over the test area: (a) observed 1950s mean (open circle), 1980s mean (closed circle), and climatology (dashed line); and (b) ensemble C (open circle) and ensemble D (closed circle). (See text for further explanation.)

observed drought occurred (Fig. 5). Over the test area the rainfall is reduced by 39 mm month^{-1}. In this paper all tabulated and mapped differences are either 1980s−1950s (for the observational data) or D−C (for simulations).

Figure 4(b) shows the internal variability in the model simulations. To quantify the statistical significance of the result a Student's t-test was conducted. In the t-test, ten JAS cases (four from 1 June 1988 initial condition, and three each from 2 June 1988 and 3 June 1988 initial conditions) were used to calculate the model internal variability in order to avoid overestimation of the statistical significance. The results of the t-test are shown in Fig. 5(b). The differences between ensembles C and D are significant at the 90% level over a large part of the test area, as shown by the shaded areas in Fig. 5(b). The rainfall deficit over west Africa is significant at the 97.5% level. Although the extent and degree of the prescribed desertification may be exaggerated in this study, the simulated rainfall anomaly is still smaller than that observed (Table 3). The implication of this discrepancy needs to be further investigated.

Further analyses show that the simulated rainfall anomaly over area N, which is 27 mm month^{-1}, is substantially lower than the observed 45 mm month^{-1}. The relatively small reduction over area N may be partially due to the under-simulation of the mean rainfall there (Fig. 2(b)). Over area S the observed and simulated rainfall anomalies are 46 mm month^{-1} and 51 mm month^{-1} respectively, which are very close. The observed JAS rainfall was enhanced in the region to the south of the Sahel, including the Gulf of Guinea and

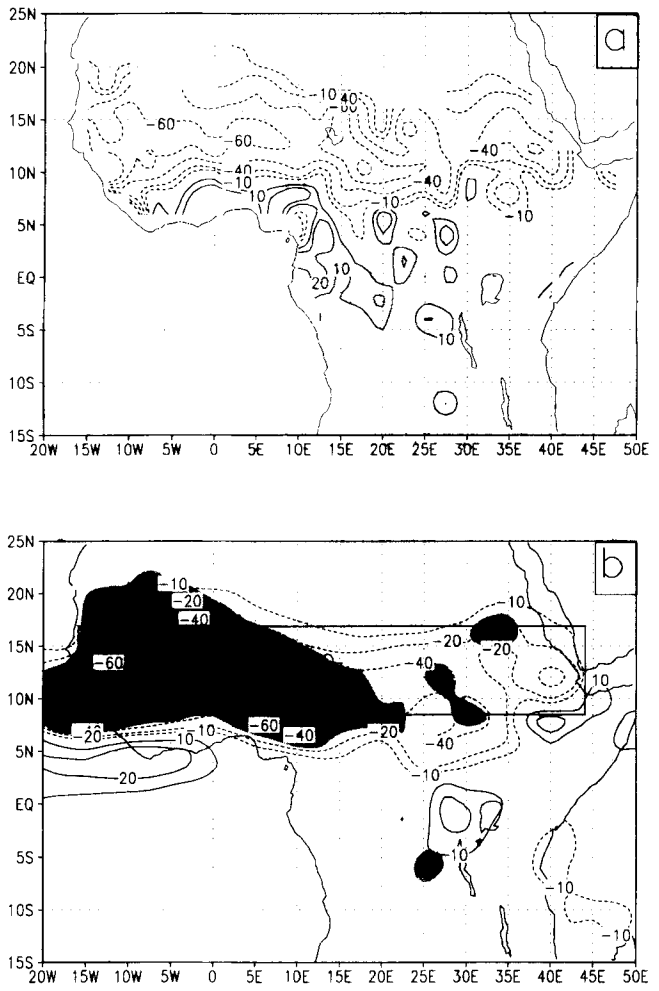

Figure 5. July to September mean precipitation differences: (a) observed rainfall differences between 1980s and 1950s and (b) ensemble D minus ensemble C. Contour levels are −60, −40, −20, −10, 10, 20 mm month^{-1}. The area enclosed by the dark line is referred to as the test area. The shading shows significance at the 90% level. (See text for further explanation.)

central Africa (Fig. 5(a)). This dipole pattern is only weakly represented by the model, and the positive anomaly along the coast of the Gulf of Guinea is not simulated. Xue and Shukla (1993, Fig. 6(a)) showed that during the 1980s the observed rainfall deficiency in the Sahel was a consequence of a 5° southward shift of the rainfall maximum, which produced a positive anomaly along the coastal area. However, in the current model simulations the mean rainfall band maximum is about 3–5° southward and too close to the coast compared with observations. Thus, this model is not able to simulate the southward shift and the positive anomaly along the coast. The simulated positive rainfall anomaly over the Gulf of Guinea and central Africa is produced by an increase in moisture flux convergence and will be discussed later.

During OND the drought area shifts to the south (Fig. 6(a)). The observed rainfall reduction area surrounding the Gulf of Guinea is well simulated with a larger rainfall reduction compared with the observations. The results are significant at the 90% level as indicated by the shaded area in Fig. 6(b). Although the amount of rainfall reduction in

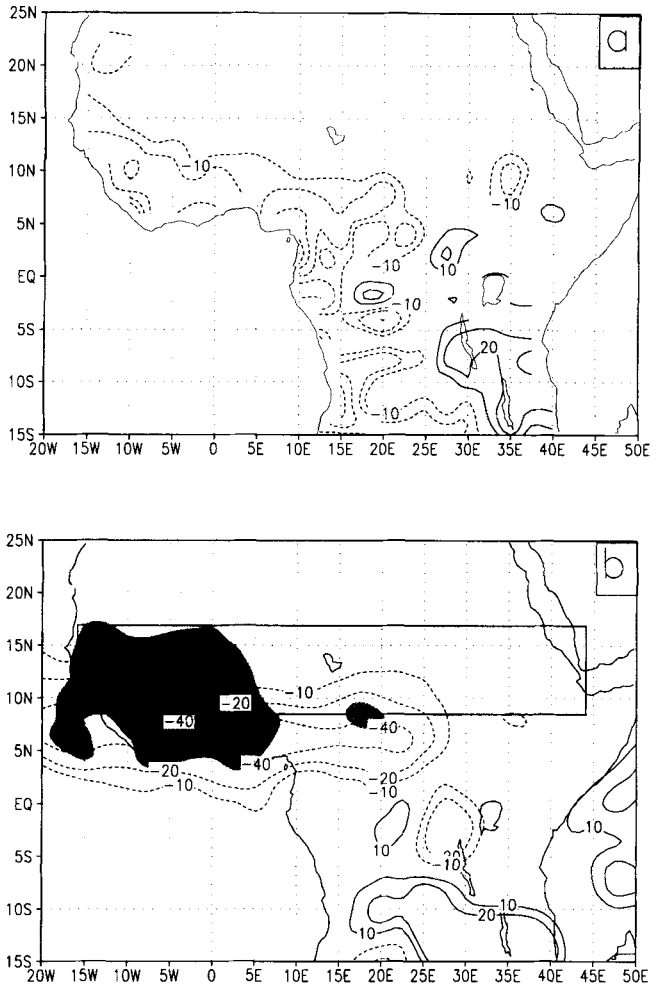

Figure 6. As Fig. 5 but for October to December.

area SW, which is located from 10°W to 25°E and 5°N to 9°N, is larger than that in area S, its relative reduction, 23%, is less than the rainfall reduction in area S, which is 33%. In eastern Africa the rainfall increased in the last decade (Nicholson 1993) mainly during OND. Figure 6(b) shows the simulation of this positive rainfall anomaly, but its position is much farther to the south and its extent is larger than observed. Evidence has shown that some wet events during the 1980s may be related to the El-Niño/Southern Oscillation (ENSO) (Rowell *et al.* 1994). The relationship between this anomaly and land-surface degradation in the Sahel needs to be further investigated.

During JFM there is very little rainfall in the Sahel, which is also simulated by the model (Fig. 4(b), Table 3). Drought conditions start to develop in the Sahel when the ITCZ moves northward during AMJ. However, the simulated rainfall reduction during AMJ is much larger than that observed (Fig. 4(b), Table 3). This over-simulation may be partially caused by the mean rainfall simulation and by the design of the desertification scenario. As shown in Table 1, the changes in the land-surface conditions in the desertification experiment were specified for the entire year. As discussed earlier, observations indicate

TABLE 4. DIFFERENCES IN SURFACE ENERGY BALANCE, PRECIPITATION AND CLOUD COVER BETWEEN ENSEMBLE D AND C (SEE TEXT)

	July to September			January to March	April to June	October to December
	Area S	Area N	Test area	Test area	Test area	Test area
Latent-heat flux	−23	−18	−21	−9	−17	−11
Sensible-heat flux	10	−8	1	−17	−13	−11
Net short-wave flux at surface	−1	−16	−9	−21	−15	−16
Net long-wave flux at surface	−12	−10	−11	−5	−15	−6
Net radiation flux at surface	−13	−26	−20	−28	−30	−22
Outgoing long-wave flux at top	10	10	10	3	10	4
Precipitation	−51	−27	−39	−6	−27	−8
Cloud cover	− 0.09	− 0.07	− 0.08	− 0.04	− 0.07	− 0.04

The units are W m^{-2} for fluxes and mm $month^{-1}$ for precipitation.

that the vegetation in this area starts to grow in May. Therefore, despite desertification, there should have been no substantial differences in land-surface conditions in this region before May. It is possible that the assigned differences in albedo (0.085) and other vegetation properties are larger than reality. Recent sensitivity studies have shown that changes in albedo have the largest impact on the model simulations, whilst changes in aerodynamic resistance have the second largest impact (Xue and Allen 1995; Xue *et al.* 1996d). Therefore the changes in albedo and other vegetation parameters during the spring may have partially caused over-simulation of the desertification impact. The over-simulation of the AMJ rainfall (Table 3) may also contribute to this problem.

5. SURFACE ENERGY BALANCE

The JAS mean surface energy components, precipitation and cloud cover for areas S and N and the test area are listed in Table 4. The latent-heat flux reduction is of the same magnitude as the net radiation loss in the test area, and is relatively uniform over the test area (Fig. 7(a)), but other energy components display different features. The net radiation flux has a larger loss in area N. This change is consistent with Xue and Shukla's (1993) result. For areas S and N the net radiation reductions in Xue and Shukla's (1993) experiment were 10 and 22 W m^{-2} respectively, which are very close to the results in this study (Table 4).

Both area S and area N have large upward short-wave radiation fluxes in the desertification experiments due to higher specified surface albedo. The loss of surface upward short-wave radiation is about 35 W m^{-2} over both areas (Figure 7(c)). It is partially compensated by the increase in incoming short-wave radiation. Less cloud cover in this area allows more short-wave radiation to reach the ground. The difference in cloud cover reduction over areas S and N is not very large; however, the impact on the two areas is quite different. Area S is located in the maximum rainfall belt, with low and middle clouds being dominant. The variations in these types of clouds have a much larger impact on short-wave radiation. Downward short-wave radiation was greatly enhanced by the reduction in cloud cover. The net short-wave radiation does not vary in area S despite the high surface albedo. Over area N only half of the short-wave radiation loss due to high surface albedo is compensated by the enhanced downward short-wave radiation. This suggests that the

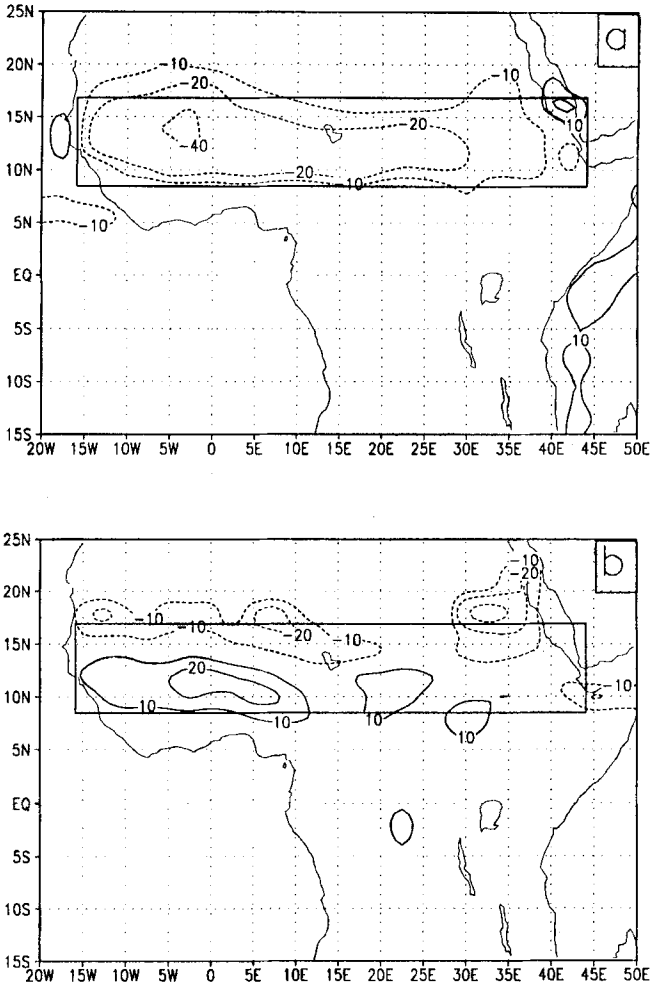

Figure 7. July to September mean difference between ensembles D and C in: (a) latent-heat flux, (b) sensible-heat flux, (c) net short-wave radiation at surface, and (d) net long-wave radiation at surface. Contour levels are −40, −20, −10, 10, 20 W m^{-2}. The area enclosed by the dark line is referred to as the test area. (See text for further explanation.)

changes in cloud cover there are mostly at high altitude in optically thin clouds with less influence on the short-wave radiation. Further analysis of the model results revealed that the net long-wave radiation loss at the surface is dominated by the reduction in downward long-wave radiation due to reduced cloud cover (Fig. 7(d)). The differences between these two areas are not substantial.

The changes in sensible-heat flux have different signs in areas S and N (Fig. 7(b)), which depend on the net radiation and latent-heat flux variations. In area S, where the net radiation at the surface changes little, the sensible-heat flux increases in ensemble D to compensate the decrease in latent-heat flux in order to balance the energy budget. In area N, where the net radiation loss is larger, both sensible-heat and latent-heat fluxes are reduced.

The changes in surface energy balance influence the surface temperature. Figure 8 shows the observed JAS mean surface air temperature at screen level and simulated surface temperature in the canopy air space. These observed temperature data are provided by

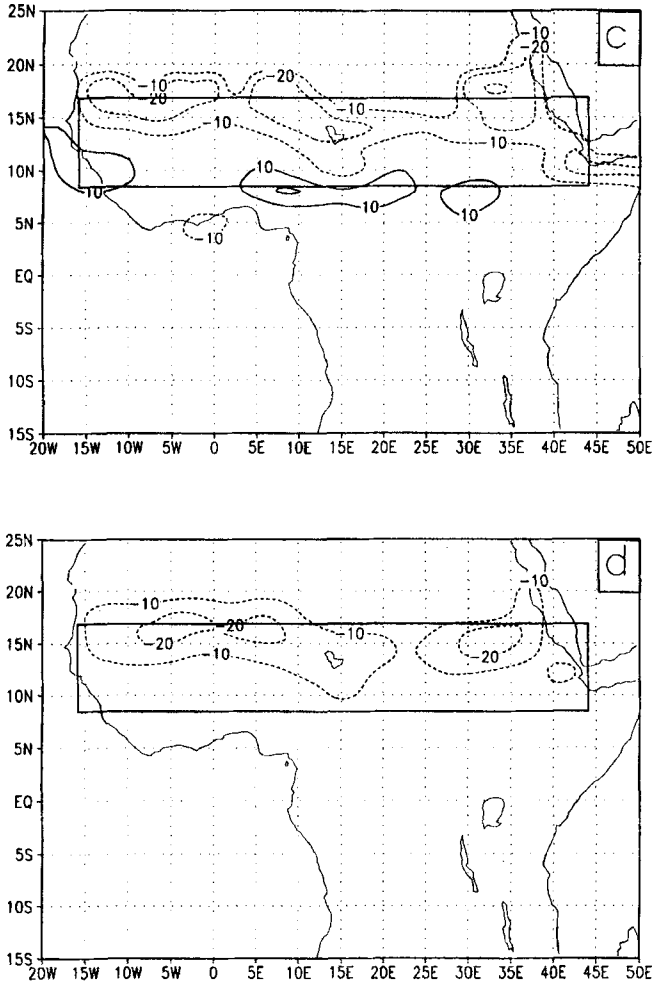

Figure 7. Continued.

Oak Ridge National Laboratory (Vose *et al.* 1992) for the study of global climate change. About 50 stations over equatorial north Africa (between 0°N and 25°N) have observational records longer than 50 years. The number of stations increased dramatically during the 1950s, when it reached about 200. During the 1980s it was reduced to about 100 stations. Many of the stations are located in west Africa and the Gulf of Guinea. Very few stations are located to the north of 16°N. The data set was quality controlled, with all unrealistic values set to missing. The Oak Ridge temperature data were interpolated to the model grid points by the same method as was used for precipitation, and a topography correction was applied (see Xue *et al.* (1996b) for details). Results shown in Fig. 8(a) are the 50-year average from 1940 through 1990. Consistent with the precipitation, the observed surface temperature has a zonal pattern in the 304, 302 and 300 K isotherms over the Sahel area (Fig. 8(a)). This pattern and the two temperature lows near the corner of the Gulf of Guinea and eastern Africa are well simulated (Fig. 8(b)), but the 298 K isotherm is about 2–3° north of its observed position. The JAS mean is close to the observed value with a slight cool bias (Table 5).

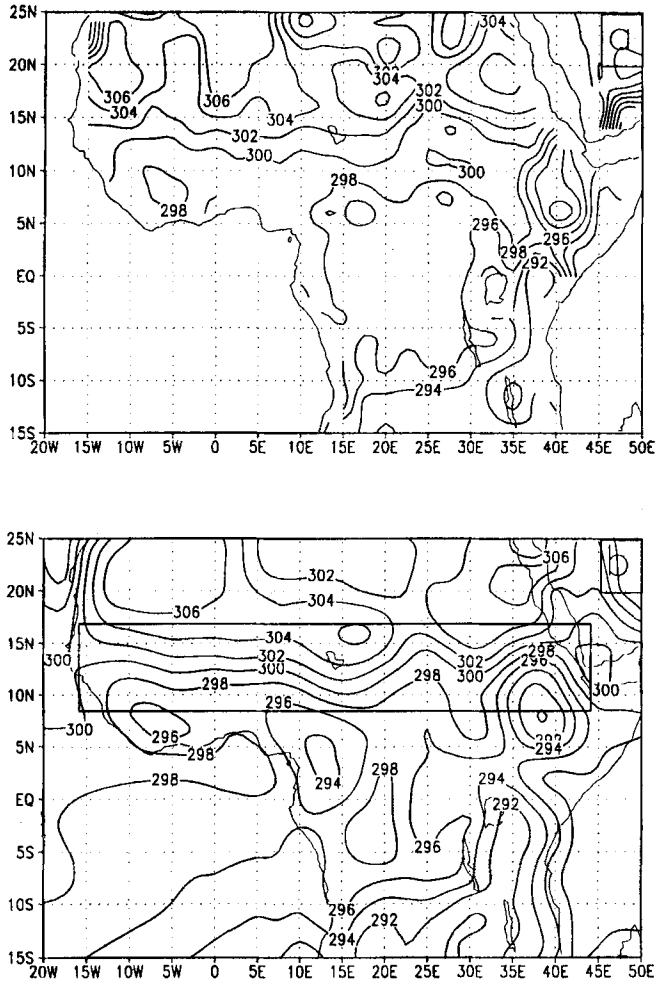

Figure 8. July to September mean surface air temperature: (a) observed and (b) ensemble C. Contour interval is 2 K. The area enclosed by the dark line is referred to as the test area. (See text for further explanation.)

TABLE 5. SEASONAL MEAN SURFACE TEMPERATURE (K) OVER THE TEST AREA (SEE TEXT)

	January to March	April to June	July to September	October to December
Observed climatology	298.7	304.3	301.4	299.2
Observed difference between the 1980s and 1950s	0.1	0.6	1.1	0.2
Simulated temperature in ensemble C	295.9	301.4	300.4	297.0
Simulated difference between ensembles D and C	− 0.9	0.3	0.8	− 0.2

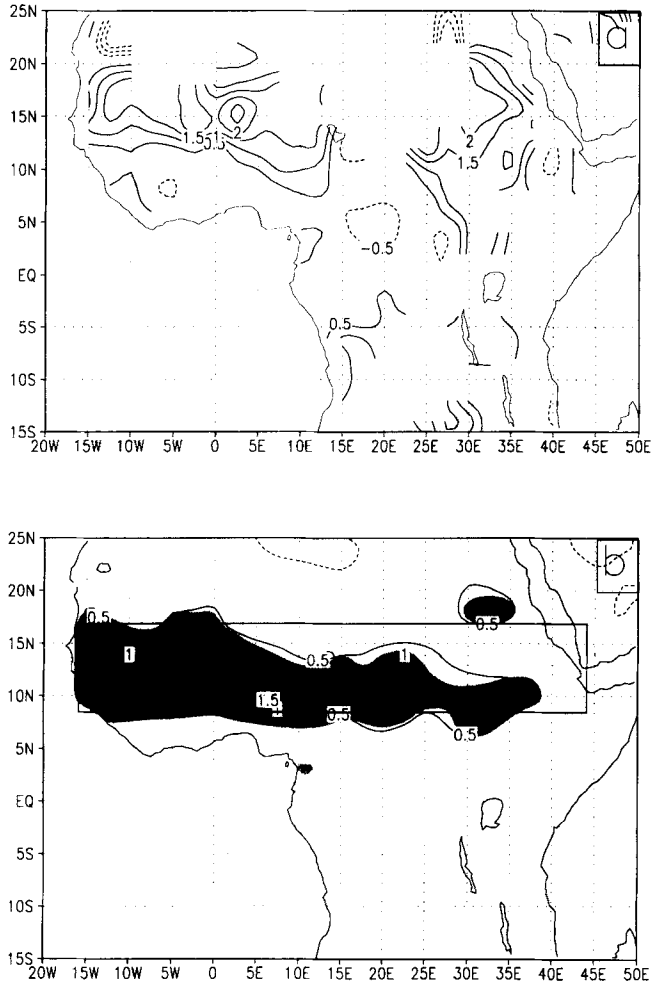

Figure 9. July to September mean surface air temperature differences: (a) observed difference between 1980s and 1950s, and (b) ensemble D minus ensemble C. Contour levels are 0.5, 1, 1.5, 2 K. The area enclosed by the dark line is referred to as the test area. Shading shows significance at the 90% level. (See text for further details.)

Observational data show that the summer surface temperature over the Sahel region increased during the 1980s (Fig. 9(a)). The simulated surface air temperature also increases in the test area where the surface energy balance is modified in the desertification experiments (Fig. 9(b)). Compared with the observations, the positive-anomaly area is about 5° south of the observed position and consistent with the maximum rainfall reduction area. The simulated surface air temperature is increased by 0.8 K (Table 5). It has a larger increase in area S, 1.1 K, where the latent-heat reduction is dominant. The temperature increase in area N is only 0.4 K. A Student's t-test was conducted to quantify the statistical significance of the results. The difference between ensembles C and D is significant at the 90% level in the shaded areas in Fig. 9(b) which almost cover all the area where the surface-air temperature difference is larger than 0.5 K. In the areas with temperature differences larger than 1 K, the statistical significance is at the 97.5% level. Similar to the situation with precipitation, most of these areas are located in western Africa.

Figure 10 shows the time series of observed and simulated surface temperatures in the canopy air space over area S, where the surface temperature differences are large. The

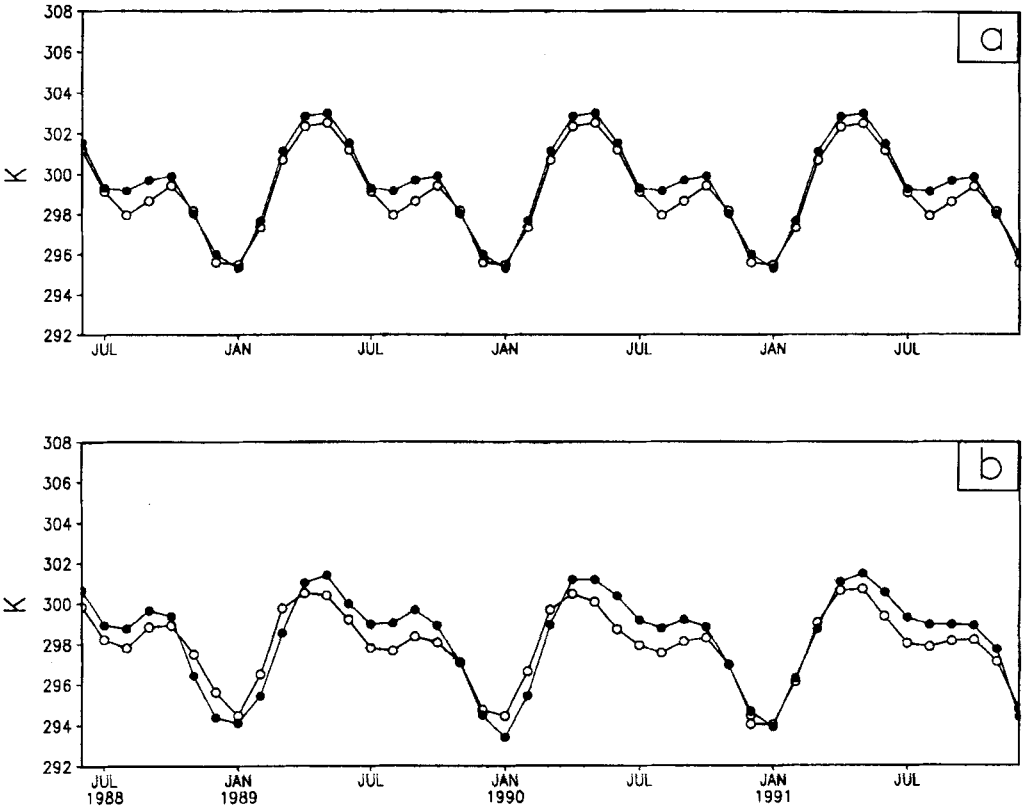

Figure 10. Monthly mean surface air temperature over area S: (a) observed 1950s mean (open circle) and 1980s mean (closed circle) and (b) ensemble C (open circle) and ensemble D (closed circle). (See text for further explanation.)

simulated seasonal variation patterns are similar to those observed: one temperature peak occurs in April and May and, when the ITCZ moves in, the surface temperature is reduced; a second peak occurs in September and October; December and January are the coldest months. The seasonal means of the observed surface temperature and simulated temperatures in canopy air space over the test area are listed in Table 5. Although the simulated JAS surface temperature and its anomaly are close to the observations, in other seasons the simulated surface-air temperature is generally lower. The reason for this systematic bias is unclear. In the observed data a substantial temperature increase (1.1 K) occurred in JAS, and a modest temperature increase (0.6 K) occurred in AMJ. The model simulates the warming well, but there is quite a large difference between the simulated temperature difference between ensemble D and C and the observations in JFM.

Table 4 lists the mean surface energy balance for JFM, AMJ, and OND in the test area. The latent-heat flux is reduced in all three of these seasons but less so than that in JAS. Unlike JAS, all three seasons had large net short-wave radiation losses. Although the albedo changes are almost constant during the year, the compensation due to cloud cover reduction is much less in these three seasons compared with that in JAS, especially in JFM which is the driest (see Table 3). The latent-heat flux only has a small change in JFM. The surface temperature decreased to maintain the model energy balance. As discussed in the last section, the discrepancy between the observed and simulated temperature anomaly may be partially caused by the unrealistic specification of desertification in this experiment.

TABLE 6. DIFFERENCES IN OCTOBER TO DECEMBER SURFACE ENERGY BALANCE AND OTHER VARIABLES BETWEEN ENSEMBLES D AND C FOR AREAS S AND SW (SEE TEXT)

	Area S	Area SW
Latent-heat flux	−17	−7
Sensible-heat flux	−10	9
Net short-wave flux at surface	−17	15
Net long-wave flux at surface	−11	−12
Net radiation flux at surface	−28	3
Outgoing long-wave flux at top	6	10
Cloud cover	−0.056	−0.088
Observed precipitation	−8	−28
Simulated precipitation	−12	−42
Vertical velocity at 500 mb	3	12
Total diabatic heating at 500 mb	−0.2	−0.6

The units are W m^{-2} for fluxes, mm $month^{-1}$ for precipitation, 10^{-5} hPa s^{-1} for pressure vertical velocity, and K day^{-1} for diabatic heating rate.

Another difference between JAS and the other three seasons is in the changes in sensible-heat flux. With large reductions in short-wave radiation absorbed and smaller reductions in latent-heat flux in these three seasons, the sensible-heat flux is also reduced. The reduction of latent-heat flux in AMJ is relatively larger, consistent with the relatively large rainfall reduction.

In OND, after the ITCZ moves to the south, only in area S does the energy budget change greatly. Table 6 lists the surface energy budgets for area SW and for the adjacent area S. The net radiation is lower in area S due to the high surface albedo during OND. It also experiences a reduction in latent-heat flux, but the surface temperature remains the same. In area SW there is little variation in surface net radiation and latent-heat flux. The reduction in short-wave radiation intercepted by the cloud cover is offset by reduced downward long-wave radiation. The changes in circulation in area SW are influenced by the variations in the test area and the drought condition simulated during JAS.

6. HYDROLOGICAL CYCLE

Consistent with the precipitation and energy-budget changes, the components of the hydrological cycle in the control and desertification experiments are profoundly different. The simulated monthly means for several variables including evapotranspiration (ET), vertically integrated moisture flux convergence (VMFC), total runoff, and VSMC in the rooting zone were averaged over the test area or area S; the results are shown in Fig. 11. All these variables have clear seasonal variations, with the peak in the summer rainy season. ET, VMFC, and their anomalies (i.e. the differences between desertification and control integrations) are highly correlated with the precipitation and its anomalies; correlation coefficients are greater than 0.93.

Unlike the VMFC and ET, there is a substantial spin-up period for surface moisture and total runoff which includes surface runoff and drainage (Figs. 11(c) and 11(d)). This did not cause a serious problem for the simulated anomalies of precipitation, ET and VMFC. Over the test area the average differences of JAS precipitation, ET, and VMFC between D and C over four years are −39, −22 and −21 mm $month^{-1}$, respectively. Their differences over three years are −42, −24, and −22 mm $month^{-1}$, respectively.

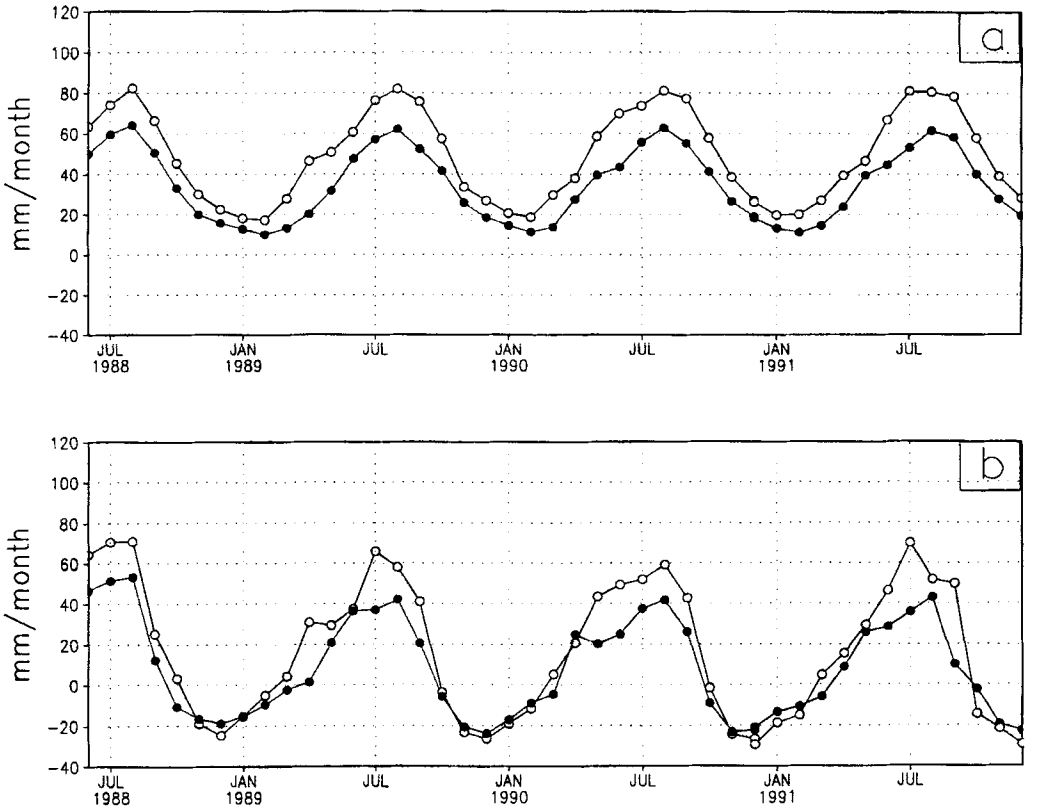

Figure 11. Monthly means: (a) evapotranspiration (mm month^{-1}) over the test area, (b) vertical integrated moisture flux convergence (mm month^{-1}) over the test area, (c) volumetric soil moisture content at rooting zone depth over the test area, and (d) total runoff over area S. Ensemble C (open circle) and ensemble D (closed circle). (See text for further explanation.)

Runoff is a very important variable in the water cycle and depends on the rainfall, vegetation cover, faunal activity, and intensity and spatial distribution of surface crusting, etc. (Casenave and Valentin 1992). The last two factors are not included in our surface model. The results for runoff presented in this study can only be viewed as a preliminary step in exploring the land-surface degradation impact.

The time series for average runoff over area S is shown in Fig. 11(d). The runoff is close to zero over area N in C and D. Unlike other variables, the simulated runoff anomaly changed sign after the first year, when the sandy soil produced larger runoff. However, this does not hold true when the transient period passes. During the remaining years of the integration, the total runoff is lowered by 9 mm month^{-1} over area S, which is consistent with the reduction in precipitation.

The soil moisture is persistently lower in the desertification experiment (Fig. 11(c)). The simulated VSMC difference at the rooting zone increased from 0.02 at the beginning of the integration to about 0.07 after one year, when it became relatively stable (Fig. 12(d)). There are seasonal variations in soil moisture. However, unlike ET and VMFC, the simulated soil moisture difference between ensembles D and C did not exhibit any substantial seasonal variations (Table 7). Based upon the results from the last three years, the correlation coefficients between JAS rainfall and the two hydrological components, runoff and soil moisture at the rooting zone over the test area, are 75% and 66%, respectively.

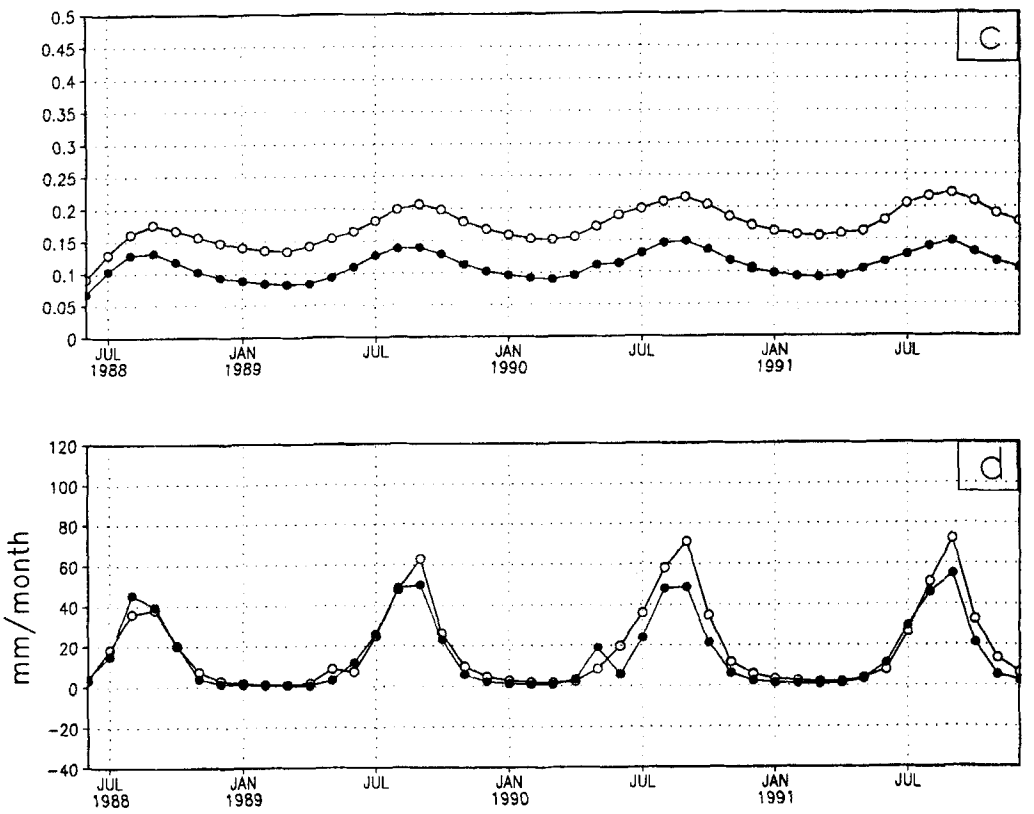

Figure 11. Continued.

The correlation coefficient between the JAS precipitation difference and runoff anomaly is 45%, and a very low value of 32% for soil moisture anomaly at the rooting zone. Only the soil moisture in the surface layer had a high correlation, 92%, with rainfall.

Table 7 lists the three-year mean changes in the atmospheric hydrological components between D and C over the test area. Over an entire year, the precipitation, ET, and moisture flux convergence (MFC) should be balanced. However, there is a slight imbalance in Table 7

TABLE 7. CHANGES IN HYDROLOGICAL COMPONENTS BETWEEN ENSEMBLES D AND C (THREE-YEAR MEAN) (SEE TEXT)

	July to September			January to March	April to June	October to December	Annual
	Area S	Area N	Test area	Test area	Test area	Test area	Test area
Precipitation	−56	−29	−42	−6	−25	−7	−20.1
Evapotranspiration	−26	−21	−24	−10	−17	−12	−15.7
Moisture flux convergence	−29	−12	−22	3	−9	6	−5.5
Runoff	−9	−1	−5	−1	0	−4	−2.5
Volumetric soil moisture content at rooting zone depth	−0.07	−0.06	−0.068	−0.064	−0.062	−0.07	−0.066
Precipitable water	−3.4	−4.4	−3.8	−2.7	−4.0	−1.9	−3.1

The units are mm month^{-1} for evapotranspiration, moisture flux convergence and runoff, and kg for precipitable water.

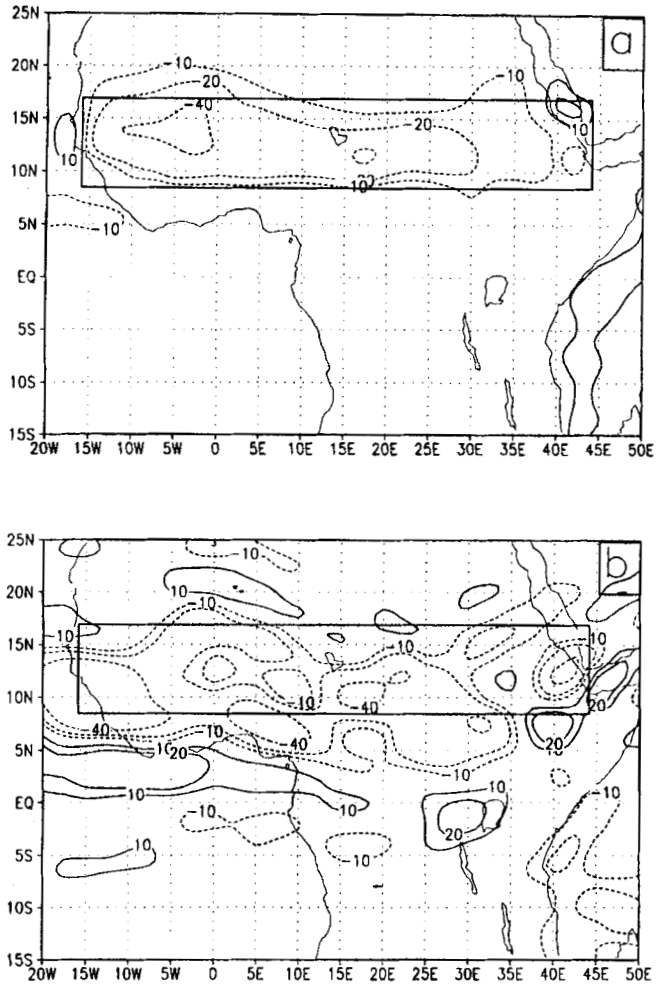

Figure 12. July to September mean differences between ensembles D and C in: (a) evapotranspiration (mm month^{-1}), (b) vertical integrated moisture flux convergence (mm month^{-1}), (c) runoff (mm month^{-1}) (contour levels for (a), (b) and (c) are −40, −20, −10, 10, 20 mm month^{-1}), and (d) volumetric soil moisture content at rooting zone depth (contour levels are −0.05, −0.075, −0.1 mm). The area enclosed by the dark line is referred to as the test area. (See text for further explanation.)

(1.1 mm month^{-1}). This is because the precipitation and ET were calculated on the model Gaussian grid, and the humidity and wind field that were used to obtain the MFC were calculated in the spectral domain. The MFC was interpolated by post-processing to the Gaussian grid which can cause large truncation errors.

At the surface, the precipitation should be balanced by the ET, runoff, and changes in soil water content. If the model reaches an equilibrium condition, the changes in soil water should be zero over a one-year period. From Table 7 it is clear that the model is not in complete equilibrium due to the model internal interannual variability and spin-up. The residual is about 1.9 mm month^{-1}. Because this model only outputs the VSMC for each soil layer, not the total soil water content, and the soil layers have different depths in each grid box, we are unable to obtain the exact instantaneous value of the total soil water content. But, based on the major vegetation types in the test area, it can be estimated that, unlike the atmosphere where the storage term is small, a small deviation of about 0.005

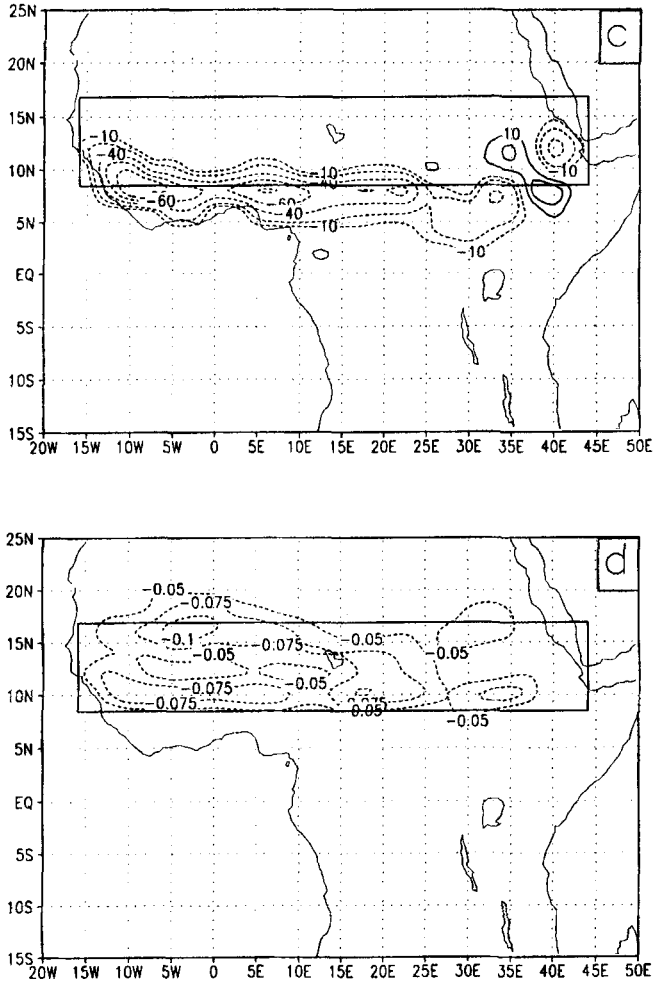

Figure 12. Continued.

in VSMC from its equilibrium condition can produce the imbalance shown in Table 7. An examination of three years of model results reveals that the magnitude of this residual is quite stable. Such small variations may be within the range of GCM's internal interannual variations.

Figures 12(a) and 12(b) show the JAS mean differences between D and C of ET and VMFC, respectively. The largest reduction in ET and VMFC (20 mm month^{-1}) occurs during JAS (Table 7). Compared with the ET, the integrated VMFC exhibits larger internal variability. The simulated anomaly patterns of ET and VMFC during JAS are similar to those in Xue and Shukla (1993); i.e. in the test area, both ET and VMFC contribute to the anomaly pattern. To the south of the test area, however, the changes of VMFC coincide with the simulated positive rainfall anomaly, with no changes in ET.

During the OND period the rainfall, ET, and VMFC over area SW are reduced by 41, 2, and 30 mm month^{-1}, respectively. To the south of area SW a positive-anomaly convergence region is coincident with a region of relative rising vertical motion (Fig. 14(b)) and the positive rainfall anomaly in eastern Africa (Fig. 6(b)). Most of the moisture in this anomaly

TABLE 8. CHANGES IN OCTOBER TO DECEMBER HYDROLOGICAL COMPONENTS BETWEEN ENSEMBLE D AND C (THREE-YEAR MEAN) FOR AREAS S AND SW (SEE TEXT)

	Area S	Area SW
Evapotranspiration	−19	−6
Moisture flux convergence	−1	−25
Runoff	−6	−29
Volumetric soil moisture content at rooting zone depth	−0.08	−0.02
Precipitable water	−3.1	−3.1

The units are mm month^{-1} for evapotranspiration, moisture flux convergence and runoff, and kg for precipitable water.

convergence region came from the Indian Ocean. Area S has a significant reduction in ET and soil moisture, while area SW experiences large anomalies in VMFC and surface runoff (Table 8).

Figure 12(c) shows the simulated JAS runoff difference between ensembles D and C. Due to the under-simulation of the precipitation over area N, the runoff mainly occurs over area S and to its south, where the average reduction is about 30 mm month^{-1}. For area S, the runoff is reduced over most parts except the high elevation area in the eastern Sahel. The runoff averaged in the west of area S (west of 30°E) is reduced by 10 mm month^{-1}, which is about 37% of the total runoff in ensemble C. The discovery here is different from Xue and Shukla (1993). It is clear that to investigate the impact on the land-surface hydrology a long-term integration is needed.

The atmosphere is drier in the desertification experiment. The mean precipitable water in JAS and OND is lower in ensemble D. Over the entire test area the reduction in atmospheric water vapour is very persistent, with a relative reduction of more than 10% throughout the atmosphere below 200 hPa. Near the surface the specific humidity is decreased by 1.2 g kg^{-1}.

7. ATMOSPHERIC ENERGY BALANCE

The alteration of the land-surface condition in D modifies the energy budget and soil water balance at the surface, which, in turn, modulates the energy budget in the atmosphere and atmospheric circulation. The latter further modifies the surface energy and water balance through feedback processes. Table 9(a) lists the differences in JAS total diabatic heating rate for different energy components at six different pressure levels averaged over the test area. The total diabatic heating of ensemble C is also listed as a reference.

The largest reduction occurs between 500 hPa and 300 hPa (Fig. 13(a)). The reduction is caused by different mechanisms, including the changes in short-wave (SW) radiative heating, long-wave (IR) radiative heating, convective latent heating, large-scale latent heating, vertical-diffusion heating, and shallow convective heating. The numbers in Table 9(a) reveal the roles of different mechanisms to reduce the total diabatic heating rate.

The differences in the vertical-diffusion heating rates and the shallow convective heating rates in Table 9(a) are negligible. The SW radiation heating rates are reduced in D.

TABLE 9(a). JULY TO SEPTEMBER HEATING RATE DIFFERENCES (K DAY^{-1}) BETWEEN ENSEMBLES D AND C OVER THE TEST AREA AT SIX PRESSURE LEVELS (SEE TEXT)

	Level (hPa)					
	850	700	500	300	200	100
Total diabatic heating rate for C	1.60	0.28	0.93	0.25	−0.18	0.17
Total diabatic heating rate difference	−0.22	−0.29	−0.58	−0.53	−0.23	0.02
Short-wave radiative heating rate difference	0.01	−0.01	−0.06	−0.07	−0.03	0
Long-wave radiative heating rate difference	−0.08	−0.01	0	0.11	0.10	0.02
Vertical diffusion heating rate difference	−0.01	−0.04	0.01	−0.01	0	0
Shallow convective heating rate difference	0	0.02	0.02	0	0	0
Convective latent heating rate difference	−0.11	−0.21	−0.49	−0.55	−0.30	0
Large-scale heating rate difference	−0.03	−0.04	−0.04	−0.01	0	0

TABLE 9(b). HEATING RATE AND VERTICAL VELOCITY DIFFERENCES AT 500 HPA OVER THE TEST AREA FOR THE FOUR SEASONS (SEE TEXT)

	January to March	April to June	July to September	October to December
Heating rate differences (K day^{-1})	−0.08	−0.44	−0.58	−0.12
Vertical velocity differences (10^{-5} hPa s^{-1})	3.7	9.8	12.9	2.4

The higher surface albedo reduces the absorption of solar radiation at the surface, and increases the reflected SW radiation to space. Less cloud cover and water vapour reduce the atmospheric absorption of SW radiation, thereby causing the SW radiation heating to decrease. The effects of the cloud reduction on IR radiation are complex. The reduction in cloud and water vapour reduces the IR radiation heating rates as in SW radiation, but increases it in the upper atmosphere. The cloud intercepts the IR flux emitted from the relatively warm surface and low atmosphere, and emits IR flux from the colder cloud top. The IR cooling rate at an optically thick cloud top can be several times larger than that in clear sky (Liou and Ou 1981).

However, the sum of these radiative changes is one order of magnitude smaller than the reduction in latent-heat heating. The difference in convective heating consists of about 85% and 100% of the total diabatic heating reduction at the 500 hPa and 300 hPa levels, respectively. The large-scale heating is also much smaller than the convective heating. In the previous section two major moisture sources that affect this convective heating, ET and moisture flux convergence, have been discussed. The cooling in the upper atmosphere (above 850 hPa) would produce sinking motion (Fig. 13(b), Fig. 14(a)). Observational data from the early 1950s to 1987 showed that the intensified large-scale subsidence over Africa is highly correlated with the decreasing trends in the Sahelian rainfall (Shinoda and Kawamura 1994). The enhanced subsidence is consistent with divergence (Fig. 12(b)), weak monsoon flow (not shown), and less precipitation as discussed in Xue and Shukla (1993). As found by the Inner Mongolian grassland experiment (Xue 1996), the patterns of relative subsidence between ensembles D and C at 500 hPa (Fig. 14(a)) and the total diabatic heating difference at 500 hPa (not shown) are very similar and highly correlated with the simulated rainfall anomalies. Less precipitation further enhances this cooling. The dynamical and thermodynamical processes support each other.

The heating rate and vertical velocity changes at 500 hPa for the four seasons are listed in Table 9(b). The large precipitation reduction (in AMJ and JAS) in D is associated

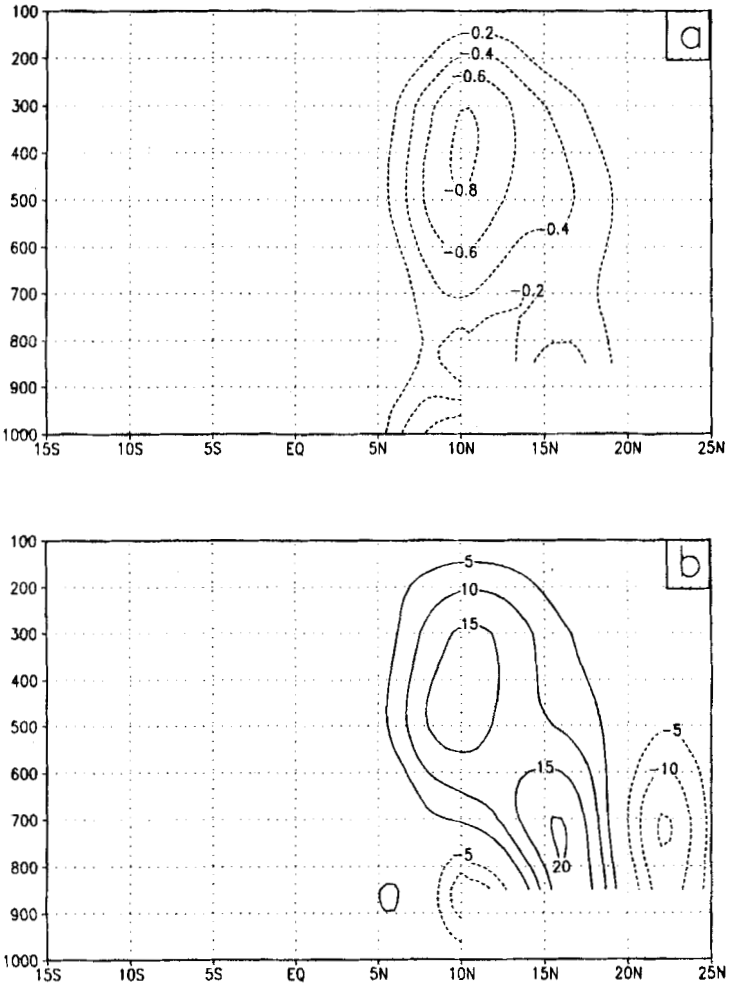

Figure 13. The zonal average differences over the African continent between ensembles D and C: (a) July to September (JAS) mean total diabatic heating rate (K day^{-1}) and (b) JAS mean vertical pressure velocity (10^{-5} hPa s^{-1}). Negative values are shown dashed. (See text for further explanation.)

with substantial reductions in heating rate and enhanced sinking motion. Comparing this table with Table 7 reveals that, although the latent-heat fluxes are changed in all four seasons, only in AMJ and JAS have the changes in latent-heat flux and MFC the same sign. This suggests that rainfall reductions in the Sahel only occur when variations in surface processes and atmospheric circulation support each other.

In OND the precipitation is also consistent with the variation in the vertical motion. Figure 14(b) is the vertical velocity difference at 500 hPa. An area of relative subsidence in the Gulf of Guinea and an area of relative rising motion in eastern Africa are consistent with the rainfall variations there; this again suggests that the convective activity is the dominant factor over these two regions.

8. Discussion and conclusions

The impact of, and mechanisms for, the land-surface degradation over the Sahel area of tropical northern Africa were investigated in this study. Two vegetation maps (climato-

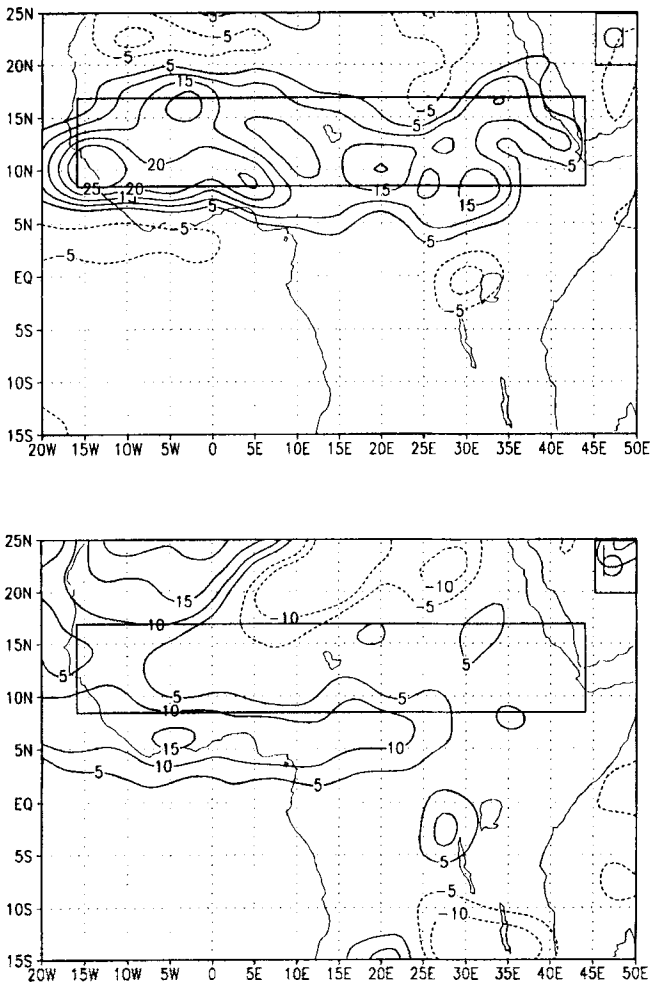

Figure 14. Mean vertical pressure velocity differences between ensembles D and C at 500 hPa: (a) July to September and (b) October to December. Contour levels: -10, -5, 5, 10, 15, 20, 25 $\times$ 10^{-5} hPa s^{-1}. The area enclosed by the dark line is referred to as the test area. (See text for further explanation.)

logical vegetation and desertification) were used in the simulations. For comparison with Xue and Shukla's (1993) results, the same specified desertification area was used. The climatological map used in this study might be different from the real vegetation distribution of the 1950s in the Sahel, and the desertification map is likely to exaggerate the real extent of land-surface degradation in the 1980s. However, if changes in vegetation properties between the 1980s and the 1950s were comparable with the specified control/desertification differences, the results indicate that the degradation could lead to regional climate changes of the order of observed differences between the 1980s and the 1950s. Results include increased surface air temperature, and reduced summer rainfall, runoff, and soil moisture over the Sahel region. The impact is not limited only to the specified desertification area and the JAS period, but it also affects the region south of this area and continues into the OND period. All these are in line with the observed climate anomalies, which suggests that the climate anomaly during the 1980s could be partially due to vegetation degradation.

Further degradation over this area may have serious consequences for the regional climate and environment.

This study, which utilizes long-term integrations, confirms many results produced from short-term integrations (Xue and Shukla 1993); in particular, the impact on atmospheric variables, such as precipitation, surface air temperature, and circulation. The calculated mean conditions in previous short-term integrations seem to be a reasonable approximation to the model-summer atmospheric climatology. The transient effects on these variables are short. This result is consistent with Charney's estimation in his GCM study (Charney 1975): about one day for dynamical adjustment and about 10 days for cloud and water vapour adjustment following a change in land-surface conditions. The short-term integrations, with relatively small computer resource requirements, provide an efficient means for sensitivity studies of these variables. However, the adjustment time for some hydrological components, such as runoff and soil water content, is much longer. A long-term integration is necessary to study the impact on these variables and, of course, the seasonal variations.

In Charney's (1975) pioneering study, using a simple dry linear model, he demonstrated that high surface albedo and friction produce strong sinking over the desert by increasing the loss of radiation to space. The atmosphere loses heat and descends adiabatically in northern Africa. Based on meteorological knowledge, it could be inferred that this sinking motion would suppress rainfall. The albedo changed from 0.14 to 0.35 in his study. Charney's hypothesis was challenged because the range of his albedo change was not supported by satellite observations (Norton *et al.* 1979; Courel *et al.* 1984). In a later GCM study, Charney *et al.* (1977) realized the defect in the model's hydrology and the importance of the hydrological cycle in feedback processes. They pointed out that the evaporation may be as important as the albedo.

With more sophisticated atmosphere and land-surface models we are able to assess more realistically the impact and mechanisms. In this, and other recent studies, the albedo changes made in the experiments were not very drastic and were within the observed range. It was found that the dominant factor, in creating the total diabatic cooling in the upper troposphere and sinking motion, is the reduction of convective heating rates; this is consistent with the decrease in latent-heat flux and moisture flux convergence. For example, Table 4 clearly demonstrates that the precipitation and the latent-heat flux from the land surface have the highest correlation compared with other surface flux components. The change in radiative heating rate was a secondary factor, although it may trigger other anomalous processes. But the anomaly was sustained by the convective processes. In a US prediction study (Xue *et al.* 1996b), even though the albedo did not change, the variation in vegetation seasonality alone was sufficient to produce precipitation and surface temperature anomalies. The change in the water cycle is the main factor that contributed to the simulated regional climate anomalies. This discovery was also confirmed by another study in which the impact of the degradation of land-surface conditions in Mongolia and the Inner Mongolian grassland on the east Asian monsoon was studied (Xue 1996).

Other African drought studies with different models have been conducted by the author and his colleagues (Xue *et al.* 1990; Xue and Shukla 1993). The June to August (JJA) reduction of precipitation, and energy and water components and increase of temperature from these two studies are listed in Table 10, where they can be compared with JJA means calculated for this study. The differences in rainfall and surface temperature between each desertification experiment and the corresponding control experiment are consistent in all three cases, despite the fact that the three studies used different models (or different versions of the model) and different integration periods; e.g. the numerical experiment in Xue *et al.* (1990) was only a one-month integration. The decrease in the sum of ET and

TABLE 10. COMPARISON OF DESERTIFICATION EFFECTS IN DIFFERENT MODELS (JUNE TO AUGUST MEANS) (SEE TEXT)

Model	Rainfall	ET	VMFC	net SW	net LW	Temperature
Xue *et al.* (1990)	−49	−47	−6	−11	−25	1.1
Xue and Shukla (1993)	−46	−19	−30	−7	−9	0.5
This study	−36	−20	−18	−9	−11	0.7

The units are W m^{-2} for net short-wave radiation (SW) and net long-wave radiation (LW); mm $month^{-1}$ for rainfall, evapotranspiration (ET), and vertical integrated moisture flux convergence (VMFC); and K for temperature.

VMFC is always very close to the reduction in precipitation. However, the partitioning between ET and VMFC is quite different and depends on the model. In the Xue *et al.* (1990) study, ET was dominant in the two-dimensional model due to the underestimation of the horizontal moisture flux convergence. The reduction of VMFC was dominant in the Xue and Shukla (1993) study, consistent with the fact that the simulated atmosphere was wetter than observed.

This study simulated the climate anomalies for JAS and OND very well, but the results for JFM and AMJ had discrepancies with those observed. In addition to the deficiencies in the models (GCM and/or surface model), the unrealistic specification in the desertification experiments played a role. Since the climate in this area is sensitive to land-surface conditions, improper specification of the land surface could cause problems, such as the ones in the US simulation (Xue *et al.* 1996b). To assess realistically the impact of land-surface degradation, more accurate knowledge of the physical and biological changes in the Sahel during pluvial and drought periods is necessary. Unfortunately, despite the fact that the importance of the land-surface conditions in the Sahel has been known since Charney's (1975) study, there is still a shortage of such information.

To overcome these problems, a few field experiments, such as the Sahelian Energy Balance Experiment (SEBEX) and the Hydrological Atmospheric Pilot Experiment in the Sahel (HAPEX-Sahel) (Wallace *et al.* 1992; Prince *et al.* 1995; Goutorbe *et al.* 1994; Kabat and Goutorbe 1996), have been conducted during recent years. The main objective of these projects was to obtain direct measurements of available energy, ET and sensible-heat flux from a typical land surface in the Sahelian environment. The observational data from these sites are currently being used to validate and calibrate the SSiB model (Xue and Allen 1995; Xue *et al.* 1996d) described in section 2. Further studies of a more realistic projection on the impact on the water and energy balance due to the land-surface degradation over this area will be conducted with the calibrated model.

The rainfall in and near the ITCZ is associated with travelling African wave disturbances (AWDs). AWDs have been detected in the GCM simulations by analysing the time variations of daily rainfall and the power spectra of mean meridional winds (Xue and Shukla 1993; Druyan and Hall 1994). Xue and Shukla (1993) demonstrated that drought conditions could reduce the intensity of easterly waves, but not the frequency. In recent GCM numerical studies, Polcher (1995) found that the difference in precipitation in the tropical deforestation experiments is explained by changes in the number of intense convective events, while their characteristic precipitation remains largely the same; this issue is not discussed in this paper. A comprehensive discussion of the relationships between land-surface processes and atmospheric events, such as AWDs, the African easterly jet, and the atmospheric circulation, is beyond the scope of this paper; they will be discussed separately.

This study was designed to focus on the land-surface impact; however, a number of data analyses and modelling studies have shown a strong link between SST anomalies and Sahel drought. Since interactions between atmosphere, land, and ocean occur in the real world, all these effects must be considered in order to assess fully the causes of the Sahel drought and the relative contribution of each component.

Acknowledgements

The author would like to thank Dr J. Shukla for supporting this study and Drs S. Nicholson and M. Hulme for providing observational precipitation data. The author would also like to thank Drs S. Allen, Y.-T. Hou, R. Koster, S. S. Ou, S. Prince, D. Rowell, and E. Schneider for helpful discussions and constructive comments on this paper, and Drs J. Kinter and D. Dewitt for suggestions on the manuscript. The author appreciates very constructive suggestions by two anonymous reviewers and Dr J. Slingo (associate editor). Special thanks go to F. J. Zeng for graphical assistance. This work was conducted under support from the National Science Foundation (NSF) through NSF grants EAR-94-05431 and ATM-93-41271, and the National Oceanic and Atmospheric Administration (NOAA) through NOAA grant NA46GP0340. Computational support was provided by the National Center for Atmospheric Research Scientific Computing Division and the National Aeronautics and Space Administration Center for Computational Sciences.

References

Akhtar-Schuster, M. 1995 'Degradationsprozesse und Desertifikation im semi-ariden Randtropischen Gebiet der Butana/Rep. Sudan', Heft 105, Gottinger Beitrage zur Land- und Forestwirtschaft in den Tropen und Subtropen

Alpert, J. C., Kanamitsu, M., Caplan, P. M., Sela, J. G., White, G. H. and Kalnay E. 1988 'Mountain induced gravity wave drag parameterization in the NMC medium-range forecast model.' Pp. 726–733 in Proceedings of the eighth conference on numerical weather prediction. Baltimore, M.D., American Meteorological Society

Casenave, A. and Valentin, C. 1992 A runoff capability classification system based on surface features criteria in semi-arid areas of West Africa. *J. Hydrol.*, **130,** 231–249

Charney, J. G. 1975 Dynamics of deserts and drought in the Sahel. *Q. J. R. Meteorol. Soc.*, **101,** 193–202

Charney, J. G., Quirk, W. K., Chow, S.-H. and Kornfield, J. 1977 A comparative study of the effects of albedo change on drought in semi-arid regions. *J. Atmos. Sci.*, **34,** 1366–1385

Courel, M. F., Kandel, R. S. and Rasool, S. I. 1984 Surface albedo and the Sahel drought. *Nature*, **307,** 528–531

Cunnington, W. M. and Rowntree, P. R. 1986 Simulations of the Saharan atmosphere-dependence on moisture and albedo. *Q. J. R. Meteorol. Soc.*, **112,** 971–999

Davies, R. 1982 'Documentation of the solar radiation parameterization in the GLAS climate model'. NASA Tech. Memo 83961

Dickinson, R., Henderson-Sellers, A., Kennedy, P. J. and Wilson, M. F. 1986 'Biosphere–atmosphere transfer schemes (BATS) for the NCAR community climate model'. NCAR/TN–275+STR

Diedhiou, A. and Mahfouf, J. F. 1995 Comparative influence of land and sea surfaces on the Sahelian drought: a numerical study. *Annales Geophysica*, **14,** 115–130

Dorman, J. L. and Sellers, P. J. 1989 A global climatology of albedo, roughness length and stomatal resistance for atmospheric general circulation models as represented by the Simple Biosphere Model (SiB). *J. Appl. Meteorol.*, **28,** 833–855

Dregne, H. E. and Chou, N. T. 1992 'Global desertification dimensions and costs'. Pp. 249–282 in Degradation and restoration of arid lands. Texas Tech. University

Dregne, H. E. and Tucker, C. J.	1988	'Desert encroachment'. Pp. 16–19 in Desertification Control Bulletin, No. 16
Druyan, L. and Hall, T. M.	1994	Studies of African wave disturbances with the GISS GCM. *J. Climate*, **7,** 261–276
Fennessy, M. J., Kinter III, J. L., Kirtman, B., Marx, L., Nigam, S., Schneider, E., Shukla, J., Straus, D., Vernekar, A., Xue, Y. and Zhou, J.	1994	The simulated Indian monsoon: A GCM sensitivity study. *J. Climate*, **7,** 33–43
Folland, C., Owen, J., Ward, M. N. and Colman, A.	1991	Prediction of seasonal rainfall in the Sahel region using empirical and dynamical methods. *J. Forecasting*, **1,** 21–56
Gormitz, V.	1985	A survey of anthropogenic vegetation changes in west Africa during the last century—climate implication. *Clim. Change*, **7,** 285–325
Goutorbe, J. P., Lebel, T., Tinga, A., Bessemoulin, P., Brouwer, J., Dolman, A. J., Engman, E. T., Gash, J. H. C., Hoepffner, M., Kabat, P., Kerr, Y. H., Monteny, B., Prince, S., Said, F., Sellers, P. and Wallace, J. S.	1994	HAPEX-Sahel: a large scale study of land–atmosphere interactions in the semi-arid tropics. *Annales Geophysica*, **12,** 53–64
Harshvardhan, Davies, R., Randall, D. A. and Corsetti, T. G.	1987	A fast radiation parameterization for general circulation models. *J. Geophys. Res.*, **92,** 1009–1016
Hellden, U.	1991	Desertification—time for an assessment? *AMBIO*, **20,** 372–383
Hou, Y.-T.	1990	'Cloud–radiation–dynamics interaction'. Ph.D. dissertation. University of Maryland. (Available from the University of Maryland, College Park, MD 20742, USA)
Hulme, M.	1992	A 1951–80 global land precipitation climatology for the evaluation of general circulation models. *Climate Dyn.*, **7,** 57–72
Kabat, P. and Goutorbe, J. P.	1996	'Hydrologic Atmospheric Pilot Experiment in the Sahel II, final report'. Department of Agrohydrology, DLO Winand Staring Center for integrated land, soil and water research, Wageningen, The Netherlands
Kinter III, J. L., Shukla, J., Marx, L. and Schneider, E. K.	1988	A simulation of the winter and summer circulations with the NMC global spectral model. *J. Atmos. Sci.*, **45,** 2486–2522
Kitoh, A., Yamazaki, K. and Tokioka, T.	1988	Influence of soil moisture and surface albedo changes over the African tropical rain forest on summer climate investigated with the MRI-GCM-I. *J. Meteorol. Soc. Jpn*, **66,** 65–85
Kuchler, A. W.	1983	World map of natural vegetation. Pp. 16–17 in *Goode's World Atlas*, 16th Edition. Rand McNally
Kuo, H. L.	1965	On formation and intensification of tropical cyclones through latent heat release by cumulus convection. *J. Atmos. Sci.*, **22,** 40–63
Lacis, A. A. and Hansen, J. E.	1974	A parameterization for the absorption of solar radiation in the earth's atmosphere. *J. Atmos. Sci.*, **31,** 118–133
Lamb, P. J.	1978	Large-scale tropical Atlantic surface circulation patterns associated with sub-Saharan weather anomalies. *Tellus*, **30,** 240–251
Lamb, P. J. and Peppler, R. A.	1991	West Africa. Pp. 121–189 in *Teleconnections linking worldwide climate anomalies*. Eds. M. Glantz, R. W. Katz and N. Nicholls. Cambridge Univ. Press
Laval, K. and Picon, L.	1986	Effect of a change of the surface albedo of the Sahel on climate. *J. Atmos. Sci.*, **43,** 2418–2429
Liou, K.-N. and Ou, S.-C. S.	1981	Parameterization of infrared radiative transfer in cloudy atmospheres. *J. Atmos. Sci.*, **38,** 2702–2716
Matthews, E.	1984	'Prescription of land-surface boundary conditions in GISS GCM II: A simple method based on high-resolution vegetation data bases'. NASA Tech. Memo. 86096
	1985	'Atlas of archived vegetation, land-use and seasonal albedo data sets'. NASA Tech. Memo. 86199
Mellor, G. L. and Yamada, T.	1982	Development of a turbulence closure model for geophysical fluid problems. *Rev. Geophys. Space Phys.*, **20,** 851–875

Nicholson, S. E. 1981 Rainfall and atmospheric circulation during drought periods and wetter years in west Africa. *Mon. Weather Rev.*, **109,** 2191–2208

1993 An overview of African rainfall fluctuations of the last decade. *J. Climate*, **6,** 1463–1466

Nicholson, S. E. and Entekhabi, D. 1986 The quasi-periodic behaviors of rainfall variability in Africa and its relationship to the southern oscillation. *Arch. Meteorol. Geophys. Bioclim.*, Ser. A **34,** 311–348

Nicholson, S. E. and Palao, I. M. 1993 A re-evaluation of rainfall variability in the Sahel. Part I. Characteristics of rainfall fluctuations. *Int. J. Climatol.*, **13,** 371–389

Norton, C. C., Mosher, F. R. and Hinton, B. 1979 An investigation of surface albedo variations during the recent Sahel drought. *J. Appl. Meteorol.*, **18,** 1252–1262

Palmer, T. N. 1986 Influence of the Atlantic, Pacific and Indian Oceans on Sahel rainfall. *Nature*, **322,** 251–253

Polcher, J. 1995 Sensitivity of tropical convection to land surface processes. *J. Atmos. Sci.*, **52,** 3143–3161

Prince, S. D., Kerr, Y. H., Goutorbe, J.-P., Lebel, T., Tinga, A., Bessemoulin, P., Brouwer, J., Dolman, A. J., Engman, E. T., Gash, J. H. C., Hoepffner, M., Kabat, P., Monteny, B., Said, F., Sellers, P. and Wallace, J. 1995 Geographical, biological and remote sensing aspects of the hydrologic atmospheric pilot experiment in the Sahel (HAPEX-Sahel). *Remote Sens. Environ.*, **51,** 215–234

Rowell, D. P. 1996 Reply to comments by Sud and Lau (1996): Further analysis of simulated interdecadal and interannual variability of summer rainfall over tropical north Africa. *Q. J. R. Meteorol. Soc.*, **122,** 1007–1013

Rowell, D. P., Ininda, J. M. and Ward, M. N. 1994 'The impact of global sea surface temperature patterns on seasonal rainfall in East Africa'. In Proceedings of the International conference on monsoon variability and prediction, 9–13 May 1994, Trieste, Italy. WMO/WCRP No. 84

Rowell, D. P., Folland, C. K., Maskell, K. and Ward, M. N. 1995 Variability of summer rainfall over tropical north Africa (1906–92): Observations and modelling. *Q. J. R. Meteorol. Soc.*, **121,** 669–704

Sato, N., Sellers, P. J., Randall, D. A., Schneider, E. K., Shukla, J., Kinter III, J. L., Hou, Y.-T. and Albertazzi, E. 1989 Effects of implementing the simple biosphere model in a general circulation model. *J. Atmos. Sci.*, **46,** 2757–2782

Sela, J. G. 1980 Spectral modeling at the National Meteorological Center. *Mon. Weather Rev.*, **108,** 1279–1292

Sellers, P. J., Mintz, Y., Sud, Y. C. and Dalcher, A. 1986 A simple biosphere model (SIB) for use within general circulation models. *J. Atmos. Sci.*, **43,** 505–531

Sellers, P. J., Shuttleworth, W. J., Dorman, J. L., Dalcher, A. and Roberts, J. M. 1989 Calibrating the simple biosphere model for Amazonian tropical forest using field and remote sensing data: Part 1. Average calibration with field data. *J. Appl. Meteorol.*, **28,** 727–759

Semazzi, F. H. M., Mehta, V. and Sud, Y. C. 1988 An investigation of the relationship between sub-Sahara rainfall and global sea surface temperatures. *Atmos.–Ocean*, **26,** 11471–11485

Shinoda, M. and Kawamura, R. 1994 Tropical rainbelt, circulation, and sea surface temperatures associated with the Sahelian rainfall trend. *J. Meteorol. Soc. Jpn*, **72,** 341–357

Slingo, J. M. 1987 The development and verification of a cloud prediction scheme for the ECMWF model. *Q. J. R. Meteorol. Soc.*, **103,** 29–43

Sud, Y. C. and Fennessy, M. 1982 A study of the influence of surface albedo on July circulation in semiarid regions using the GLAS GCM. *J. Climatol.*, **2,** 105–125

Sud, Y. C and Lau, W. K.-M. 1996 Comments on 'Variability of summer rainfall over tropical north Africa (1906–92): Observations and modelling' by Rowell *et al.* (1995). *Q. J. R. Meteorol. Soc.*, **122,** 1001–1006

Sud, Y. C., Shukla, J. and Mintz, Y. 1988 Influence of land surface roughness on atmospheric circulation and rainfall: a sensitivity study with a general circulation model. *J. Appl. Meteorol.*, **27,** 1036–1054

Tiedtke, M. 1984 The effect of penetrative cumulus convection on the large-scale flow in a general circulation model. *Beitr. Phys. Atmos.*, **57,** 216–239

UNEP 1992 *World atlas of desertification.* Edward Arnold, Sevenoaks, UK

Vose, R. S., Keim, R., Schmoyer, R. L., Karl, T. R., Steuer, P. M., Eischeid, J. K. and Peterson, T. C. 1992 'The global historical climatology network: long-term monthly temperature, precipitation, sea level pressure, and station pressure data'. ORNL/CDIAC-53, NDP-041

Walker, J. and Rowntree, P. R. 1977 The effect of soil moisture on circulation and rainfall in a tropical model. *Q. J. R. Meteorol. Soc.*, **103,** 29–46

Wallace, J. S., Allen, S. J., Culf, A. D., Dolman, A. J., Gash, J. H. C., Holwill, C. J., Lloyd, C. R., Stewart, J. B., Wright, I. R., Sivakumar, M. V. K. and Renard, C. 1992 'SEBEX: The Sahelian energy balance experiment'. Final report on ODA project T06050C1. Institute of Hydrology, UK

Willmott, C. J. and Klink, K. 1986 'A representation of the terrestrial biosphere for use in global climate studies'. Pp. 109–112 in *ISLSCP* conference proceedings, Rome, Italy, European Space Agency

Xue, Y. 1991 A two-dimensional coupled biosphere–atmosphere model and its application. *Adv. Atmos. Sci.*, **8,** 447–458

1996 The impact of desertification in the Mongolian and the Inner Mongolian grassland on the regional climate. *J. Climate*, **9,** 2173–2189

Xue, Y. and Allen, S. 1995 'Testing a biosphere model (SSiB) for the Sahelian semi-arid area using field data'. Pp. 93–98 in Preprints of 1995 AMS conference on hydrology, 15–20 January 1995, Dallas, Texas

Xue, Y. and Shukla, J. 1993 The influence of land surface properties on Sahel climate. Part I: desertification. *J. Climate*, **6,** 2232–2245

1996 The influence of land surface properties on Sahel climate. Part II: afforestation. *J. Climate*. **9,** 3260–3275

Xue, Y., Liou, K.-N. and Kasahara, A. 1990 Investigation of the biophysical feedback on the African climate using a two-dimensional model. *J. Climate*, **3,** 337–352

Xue, Y., Sellers, P. J., Kinter III, J. L. and Shukla, J. 1991 A simplified biosphere model for global climate studies. *J. Climate*, **4,** 345–364

Xue, Y., Bastable, N., Dirmeyer, P. and Sellers, P. 1996a Sensitivity of simulated Amazonian climate to changes in land surface parameterization—a study using ABRACOS data. *J. Appl. Meteorol.*, **35,** 386–400

Xue, Y., Fennessy, M. J. and Sellers, P. J. 1996b Impact of vegetation properties on US weather prediction. *J. Geophys. Res.*, **101, D3,** 7419–7430

Xue, Y., Zeng, F. J. and Schlosser, C. A. 1996c SSiB and its sensitivity to soil properties—a case study using HAPEX-Mobilhy data. *Global and Planetary Change*, **13,** 183–194

Xue, Y., Elbers, J., Zeng, F. J. and Dolman, A. J. 1996d GCM parameterization for Sahelian land surface processes. In *HAPEX-Sahel west central supersite: Methods, measurements and selected results.* Eds. P. Kabat, S. Prince and L. Prihodko. DLO Winand Staring Center for integrated land, soil and water research, Wageningen, The Netherlands